AGU PUBLICATIONS

JGR

Journal of Geophysical Research: Earth Surface

RESEARCH ARTICLE

10.1002/2014JF003201

Key Points:
- Seismic records near rivers are sensitive to turbulent flow velocities
- Our model allows separating bedload from turbulent flow induced noise
- For an identified turbulent flow signal, riverbed stress can be inverted

Correspondence to:
F. Gimbert,
gimbertf@caltech.edu

Citation:
Gimbert, F., V. C. Tsai, and M. P. Lamb (2014), A physical model for seismic noise generation by turbulent flow in rivers, *J. Geophys. Res. Earth Surf.*, *119*, 2209–2238, doi:10.1002/2014JF003201.

Received 5 MAY 2014
Accepted 15 SEP 2014
Accepted article online 18 SEP 2014
Published online 16 OCT 2014

A physical model for seismic noise generation by turbulent flow in rivers

Florent Gimbert[1,2], Victor C. Tsai[1,2], and Michael P. Lamb[2]

[1]Seismological Laboratory, California Institute of Technology, Pasadena, California, USA, [2]Division of Geological and Planetary Sciences, California Institute of Technology, Pasadena, California, USA

Abstract Previous studies suggest that the seismic noise induced by rivers may be used to infer river transport properties, and previous theoretical work showed that bedload sediment flux can be inverted from seismic data. However, the lack of a theoretical framework relating water flow to seismic noise prevents these studies from providing accurate bedload fluxes and quantitative information on flow processes. Here we propose a forward model of seismic noise caused by turbulent flow. In agreement with previous observations, modeled turbulent flow-induced noise operates at lower frequencies than bedload-induced noise. Moreover, the differences in the spectral signatures of turbulent flow-induced and bedload-induced forces at the riverbed are significant enough that these two processes can be characterized independently using seismic records acquired at various distances from the river. In cases with isolated turbulent flow noise, we suggest that riverbed stress can be inverted. Finally, we validate our model by comparing predictions to previously reported observations. We show that our model captures the spectral peak located around 6–7 Hz and previously attributed to water flow at Hance Rapids in the Colorado River (United States); we also show that turbulent flow causes a significant part of the seismic noise recorded at the Trisuli River in Nepal, which reveals that the hysteresis curve previously reported there does not solely include bedload, but is also largely influenced by turbulent flow-induced noise. We expect the framework presented here to be useful to invert realistic bedload fluxes by enabling the removal of the turbulent flow contribution from seismic data.

1. Introduction

Water flow in rivers is governed by gravitational forces that drive flow downslope and forces due to frictional resistance at the riverbed and banks. Frictional forces at the riverbed are, in turn, major controls on flow velocity, flow depth, and the rate of sediment transport [e.g., *Manning*, 1891; *Bagnold*, 1966; *Einstein and Barbarossa*, 1952]. In bedrock-beded rivers, these frictional forces also control the rate of bedrock erosion by plucking of fractured rock and abrasion by impacting particles traveling in bedload or suspended load [e.g., *Whipple et al.*, 2000; *Sklar and Dietrich*, 2004; *Lamb et al.*, 2008a]. Fluvial bedrock erosion, in turn, drives the evolution of landscapes with broad implications for the interplay between tectonics, climate, and topography [e.g., *Howard and Kerby*, 1983; *Whipple*, 2004; *Egholm et al.*, 2013]. Direct and continuous measurements of near-bed hydraulic forces and sediment transport are notoriously difficult to make, especially in mountain streams, and there is a need to develop new methods to monitor rivers remotely [*Rickenmann and Recking*, 2011; *Rickenmann et al.*, 2012; *Turowski and Rickenmann*, 2011].

Rivers generate ground vibrations over a wide range of frequencies that may be due to particle collisions during sediment transport, waves at the free surface, cavitation, and frictional forces due to turbulent water flow acting against the riverbed and banks, for example. Recent work has shown the potential of using seismic devices to record ground vibrations near rivers to infer river hydrodynamics and sediment transport [*Govi et al.*, 1993; *Burtin et al.*, 2008, 2011; *Hsu et al.*, 2011; *Schmandt et al.*, 2013; *Díaz et al.*, 2014; *Roth et al.*, 2014]. These studies report a strong correlation between seismic noise amplitude recorded at 1–100 Hz frequencies and river discharge and suggest that such an observation technique could be used to monitor force fluctuations at the riverbed. In particular, the sensitivity of these observations to bedload transport is strongly supported by the observed hysteresis behavior of seismic noise power versus water discharge. However, since the relative contribution of water flow and bedload to the generation of seismic noise could not be evaluated in these previous investigations, our current understanding of observed seismic noise levels in terms of associated flow rates and/or sediment fluxes remains limited.

In order to invert seismic records for river hydrodynamics and sediment transport, we need mechanistic theories for the processes that generate noise in rivers, and to date only the process of noise generation by

bedload transport has been modeled [*Tsai et al.*, 2012]. The modeling work of *Tsai et al.* [2012] demonstrates that observed ground motion can be explained by a bedload seismic source, characterized by a multiplicity of single grain impact events. On the basis of this framework, bedload transport flux can be inverted from seismic observations. However, *Tsai et al.* [2012] did not consider water flow as a source of noise. A model for water flow generated noise in rivers is needed to isolate the signal of sediment transport from seismic data and to quantitatively invert for bed stress. The goal of this paper is to provide such a model.

The seismic signature of water flow noise has been investigated previously at two different study sites, one in the small braided alpine stream of the "Torrent de St. Pierre" [*Burtin et al.*, 2011] and the other in the Colorado River in the Grand Canyon [*Schmandt et al.*, 2013]. These specific studies, performed by deploying seismometers relatively close to the river channel (meters to tens of meters away), show that the low-frequency (e.g., around 10 Hz or lower) part of the ground velocity spectrum is mainly due to water flow-induced noise. At these low frequencies, *Schmandt et al.* [2013] reported no hysteresis with respect to water discharge and *Burtin et al.* [2011] observed a maximum correlation of ground velocity power with local flow depths. However, neither of these studies was able to mechanistically describe and predict the cause of water flow-induced seismic noise.

Of the possible mechanisms that may generate ground motion from water flow, here we focus on the generation of seismic waves in the 1–100 Hz frequency range from frictional forces at the riverbed due to turbulent river flow interacting with boundary roughness caused by coarse sediment. We focus on this mechanism because (1) no models yet exist for water flow generated seismic noise and we need a starting point, (2) bed shear stress is of interest due to its role in determining river hydraulics, sediment transport, and bedrock erosion, and (3) because we believe it may be the most important water flow noise generation mechanism for the 1–100 Hz frequency range (as discussed below). Near-bed turbulence may generate noise outside of the 1–100 Hz range (e.g., due to coherent flow structures [*Nikora*, 2011; *Marquis and Roy*, 2013; *Venditti et al.*, 2013]); however, here we focus on the 1–100 Hz frequency range because (1) it overlaps with observations of putative water flow-induced noise [*Burtin et al.*, 2008, 2011; *Schmandt et al.*, 2013]; (2) it overlaps with observations of putative bedload-induced noise [*Burtin et al.*, 2008, 2011; *Hsu et al.*, 2011] for which a model for water flow-induced noise is needed to isolate the bedload signal; and (3) it is the spectral range in most rivers where turbulent flow theory is particularly well developed (i.e., the inertial subrange [*Kolmogorov*, 1941]). In addition to near-bed frictional forces, sound waves generated within the water layer are expected to be converted to seismic waves at the water-ground boundary. Potential sources of sound may include cavitation [*Whipple et al.*, 2000], i.e., the implosion of air bubbles, and/or the fluctuating internal stresses in the water caused by turbulent flow, commonly called aerodynamic or hydrodynamic sound [*Lighthill*, 1952; *Curle*, 1955]. Our preliminary analysis of the hydrodynamic sound contribution to seismic noise suggests that the induced power is to be orders of magnitude lower than recorded, and thus can be ignored relative to other sources. It is important to notice, however, that hydrodynamic sound certainly significantly affects the water flow-induced noise recorded by high-frequency acoustic sensors deployed in situ, such as microphones [*Belleudy et al.*, 2010], but these measurements are distinct from ground motion measured by seismometers.

Water flow-generated ground motion may also come from processes occurring at the river's free surface. *Schmandt et al.* [2013] suggested that fluid-air interactions such as breaking waves, recorded in the air by microphone measurements, may generate significant seismic noise in the frequency range of interest. Moreover, large boulders, boulder clusters, or bedrock steps may induce gravity waves and generate pressure fluctuations at bed. Estimates of the wavelengths associated with gravity waves expected in Hance Rapids of Grand Canyon (United States) suggest that seismic noise caused by these waves is likely to operate at frequencies lower than 1 Hz, which is outside of our spectral range of interest. Wave breaking and capping, however, have relevant timescales that may strongly depend on wave size and are not well constrained. Though we do not have evidence as to whether breaking waves are likely or not to generate significant seismic noise in the 1 to 100 Hz frequency range, we do not account for this process in the present study.

The next section of this paper presents a new model for seismic noise generation by forces at the riverbed caused by the interaction of turbulent flow and boundary roughness. Section 3 explores the model results in terms of peak frequency and amplitude for water flow-generated noise at the Trisuli River, Nepal, and compares results to the bedload transport generated noise model of *Tsai et al.* [2012]. In section 4 we apply the model to the field measurements of *Schmandt et al.* [2013] at Hance Rapids on the Colorado River. We

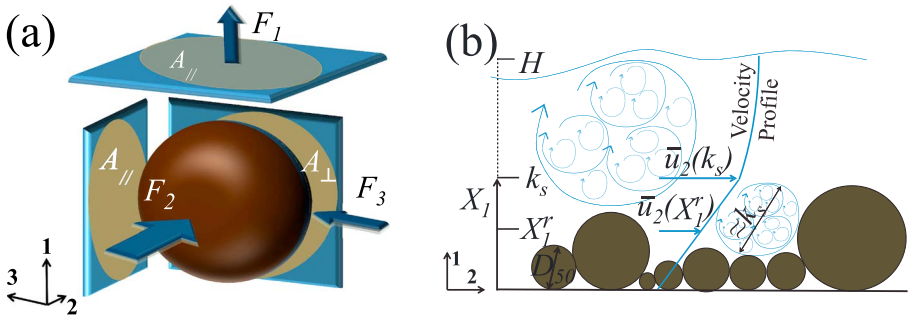

Figure 1. Schematics for the model. (a) Three-dimensional representation of the different fluctuating components of forces acting on a given riverbed grain. These forces act on the perpendicular areas associated with the different directions. (b) Two-dimensional representation of the average velocities and turbulent flow structures considered in the model. A velocity profile that deviates from the usual logarithmic profile (see equation (8)) sets the average velocities within the bed roughness. The model analysis is conducted at the reference height X_1^r at which we consider turbulent eddies with a correlation length l_c of the order of the roughness scale k_s and traveling downstream at an average velocity $\bar{u}_2\left(X_1^r\right)$. The turbulent intensity carried by these eddies is proportional to the macroscopic shearing rate of the water layer within the bed roughness.

show that the amplitude and spectral properties of forces applied by the turbulent flow on riverbed grains, up to now only measurable in dedicated flume experiments [*Nelson et al.*, 2001; *Schmeeckle et al.*, 2007], can be monitored in the field using seismic observations. From knowledge of hydrological parameters at Hance Rapids, specific features of the seismic observations reported by *Schmandt et al.* [2013] can be predicted by the water flow-induced noise model we propose. Also, the strong dependency of our model predictions on local water flow depth supports the fact that local water flow depth or bed shear stress can be inverted from seismic measurements.

2. Model

In this section, we present the derivation of a mechanical model accounting for the first-order physics that generates water flow-induced seismic noise in rivers in the 1–100 Hz frequency band due to turbulent water flow interacting with roughness along the riverbed. Refer to Appendix Notation for a summary of all variables, physical quantities, and mathematical functions defined in the following derivation.

In this model, we aim to calculate the total noise power spectral density (PSD) generated at a given seismic station from stresses applied by the flow-moving past spherical riverbed grains of various sizes. We assume that the riverbed roughness is dominated by grain-scale roughness and that all grain sizes on the bed can be transported, which is typical for gravel-bed rivers (e.g., *Parker* [1991]). As a consequence, we disregard rivers exhibiting step-pool morphology or bedforms, for which we do not expect our model to be applicable. Pressure differentials caused by turbulent flow create normal and shear stresses at all locations along the surface of any exposed grain. The average force resulting from the contribution of all stresses applied to a given grain is commonly described as a combination of an average drag force $\bar{F}_D$ and an average lift force $\bar{F}_L$. To describe these forces, we introduce the three dimensional Cartesian coordinate system with directions 1 (vertical), 2 (downstream), and 3 (cross stream) (see Figure 1). The drag and lift forces are defined with respect to an average streamwise velocity $\bar{u}_2(X_1)$ operating at elevation $X_1 = D/2$ above the bed where D is the grain diameter (i.e., $\bar{u}_2(X_1)$ is aligned with the grain center) and far enough upstream of the considered grain so that the velocity field is not disturbed [*Nelson et al.*, 2001; *Schmeeckle et al.*, 2007]. $\bar{F}_D$ acts parallel to $\bar{u}_2(X_1)$ over the normal surface $A_\perp$, which corresponds to the projection of the grain on the plane whose normal is direction 2, while $\bar{F}_L$ acts perpendicular to $\bar{u}_2(X_1)$ over the parallel surface $A_\parallel$, which corresponds to the projection of the grain on the plane with normal direction 1 [*Schlichting*, 1979; *Schmeeckle et al.*, 2007] (see Figure 1a). $\bar{F}_D$ and $\bar{F}_L$ can be written as

$$\bar{F}_D = \bar{C}_D \frac{\rho_w \bar{u}_2(X_1)^2}{2} A_\perp \quad ; \quad \bar{F}_L = \bar{C}_L \frac{\rho_w \bar{u}_2(X_1)^2}{2} A_\parallel, \tag{1}$$

where $\rho_w = 1500$ kg m^{-3} is the density of water and $\bar{C}_D$ and $\bar{C}_L$ are the average, standard, drag, and lift coefficients [*Schlichting*, 1979]. For simplicity, we assume that riverbed grains are entirely exposed to the flow, and that the area A in the case of the considered spherical particles is $A = A_\perp = A_\parallel = \pi D^2/4$.

The validity of the average drag formulation of equation (1) in open channel flow configurations is supported by laboratory measurements [*Nelson et al.*, 2001; *Schmeeckle et al.*, 2007] that report a strong linear scaling between the measured average force $\bar{F}_D$ and the square of the measured average velocity $(\bar{u}_2(X_1))^2$. However, these same experiments do not report a significant scaling between the average lift force and the average streamwise velocity difference across the grain [*Nelson et al.*, 2001; *Schmeeckle et al.*, 2007], suggesting that the Bernoulli effect caused by the average velocity gradient may not be the dominant mechanism that controls the average lift force.

Seismic waves are not generated by the average forces applied on riverbed grains but instead are generated by the fluctuating forces. On the basis of laboratory measurements conducted in an open channel flow, *Schmeeckle et al.* [2007] showed that a similar description as used for the average drag force (see equation (1)) also can be used for the instantaneous drag force $F_D(t) = \bar{F}_D + F'_D(t)$, where $F'_D(t)$ corresponds to the fluctuating drag force. An instantaneous drag coefficient C_D can be defined such that

$$\frac{F_D(t)}{A} = C_D \frac{\rho_w (u_2(t, X_1))^2}{2}, \tag{2}$$

where $u_2(t, X_1)$ is the instantaneous streamwise velocity that operates directly upstream of the grain (typically one particle diameter upstream). To our knowledge, an equivalent description for the fluctuating lift force has never been proposed, and a relevant instantaneous velocity that correlates with the instantaneous lift force could not be identified in the previous experiments of *Schmeeckle et al.* [2007]. Moreover, in addition to drag and lift, cross-stream force fluctuations (acting along direction 3, see Figure 1) are also expected to generate seismic waves.

In order to understand how the three components of fluctuating forces are incorporated into our analysis, it is convenient to first formalize the role that these different force components have in generating ground motion. From the instantaneous force history $F_i(t, \mathbf{x}_0)$ applied along direction i on a given grain g located at $\mathbf{x}_0$ in the channel, the ground velocity time series $\dot{u}_p^g(t, \mathbf{x})$ along direction p and at location $\mathbf{x}$ outside the channel can be described from *Aki and Richards* [2002] by

$$\dot{u}_p^g(t, \mathbf{x}) \equiv \sum_{i=1}^{3} F_i(t, \mathbf{x}_0) \otimes \frac{\mathrm{d}G_{pi}(t, \mathbf{x}; \mathbf{x}_0)}{\mathrm{d}t}, \tag{3}$$

where $G_{pi}(t)$ is the displacement Green's function that converts the force applied along direction i at $\mathbf{x}_0$ into ground displacement along direction p in $\mathbf{x}$, and $\otimes$ stands for time convolution. We denote the power spectral density (PSD) of the ground velocity time series $\dot{u}_p^g$ as $P_{w_p}^g$, where subscript w will be used throughout to refer to water induced seismic noise as opposed to subscript b for bedload. $P_{w_p}^g(f, \mathbf{x})$ is defined in the frequency domain as

$$P_{w_p}^g(f, \mathbf{x}) \equiv \frac{\overline{[\dot{u}_p^g(t, \mathbf{x})]_f^2}}{df}, \tag{4}$$

where $\overline{[\dot{u}_p^g(t)]_f^2}$ is the mean-square value of the time series $\dot{u}_p^g(t)$ once band-pass filtered within a frequency band df centered around the frequency f. The explicit role of the different force components in setting $P_{w_p}^g(f, \mathbf{x})$ can be seen by substituting equation (3) into equation (4), which leads to

$$P_{w_p}^g(f, \mathbf{x}) = 4\pi^2 f^2 \cdot \sum_{i=1}^{3} \sum_{j=1}^{3} \frac{\overline{\left[F_i(t, \mathbf{x}_0) F_j(t, \mathbf{x}_0)\right]_f}}{df} G_{pi}(f, \mathbf{x}; \mathbf{x}_0) G_{pj}(f, \mathbf{x}; \mathbf{x}_0), \tag{5}$$

where $G_{pi}(f) \equiv \mathcal{F}\left[G_{pi}(t)\right]$ is the Fourier transform of $G_{pi}(t)$. From equation (5), it can be seen that all three force components (i.e., i=1, 2 and 3) potentially contribute to each component p of ground motion. In addition, the ground motion power in direction p is also affected by the mean-square of the cross products of the force components. Since the turbulent flow field is likely to be correlated up to the grain scale (see section 2.1), one would expect that the force fluctuations in the various directions are correlated with each other. However, little is known about the extent to which the instantaneous forces in the three directions are correlated, nor it is known how the degree of correlation depends on frequency. Consequently, we make

the simplifying assumption that the different forces applied in the different directions vary independently of each other. In that case, the terms with $i \neq j$ in equation (5) vanish and the PSD $P^g_{w_p}(f, \mathbf{x})$ becomes

$$P^g_{w_p}(f, \mathbf{x}) = 4\pi^2 f^2 \sum_{i=1}^{3} S^g_{F_i}(f, \mathbf{x}_0) G_{pi}(f, \mathbf{x}; \mathbf{x}_0)^2, \tag{6}$$

where $S^g_{F_i}(f, \mathbf{x}_0) = \frac{\overline{[F_i(t,\mathbf{x}_0)]^2_f}}{df}$ is the PSD of the force time series $F_i(t, \mathbf{x}_0)$ acting on a given grain. The total PSD $P^T_{w_p}(f, \mathbf{x})$ resulting from the contribution of all riverbed grains can be calculated by integrating the contribution of force time series $F_i(t, \mathbf{x}_0)$ over the full grain size distribution and the full length of river R as

$$P^T_{w_p}(f, \mathbf{x}) = \int_R \int_D 4\pi^2 f^2 \sum_{i=1}^{3} S_{F_i}(f, \mathbf{x}_0; D) G_{pi}(f, \mathbf{x}; \mathbf{x}_0)^2 \mathrm{d}D\mathrm{d}\mathbf{x}_0, \tag{7}$$

where $S_{F_i}(f, \mathbf{x}_0; D)$ is the PSD of the force time series per unit length and per unit D.

We proceed with our formulation for the PSDs $S^g_{F_i}$ and S_{F_i} for i equals 1, 2, and 3 by first calculating the PSD $S^g_{F_2}$ of the fluctuating drag forces, since an appropriate description of the instantaneous drag force time series exists (see equation (2)). Then we address the cases $i = 1$ and $i = 3$ by assuming that the PSD $S^g_{F_1}$ of the fluctuating lift forces and the PSD $S^g_{F_3}$ of the fluctuating cross-stream forces applied on a given grain are similar to the PSD $S^g_{F_2}$. This assumption is motivated by the fact that the frequency scaling exhibited by the Fourier spectrum of turbulent velocities is similar in any direction in the case of isotropic turbulence as considered here [*Kolmogorov*, 1941]. Thus, the frequency scaling of the force spectrum induced by these turbulent velocities is also expected to be similar in any direction. Furthermore, in a unidirectional flow, the downstream mean flow sets the production rate of turbulent kinetic energy through shear in the boundary layer, making turbulence in all three directions sensitive to the downstream velocity [*Tennekes and Lumley*, 1972]. The assumed direct correlation between the amplitude of lift and cross-stream force fluctuations and the streamwise velocity is supported by experiments performed on particles of various shapes immersed in a three-dimensional turbulent flow advected at a given average velocity [*Vickery*, 1966; *Norberg*, 2003; *Naudascher and Rockwell*, 2005]. The assumption of similar amplitudes for $S^g_{F_1}$ and $S^g_{F_3}$ as compared to $S^g_{F_2}$ is also consistent with the measurements reported by *Schmeeckle et al.* [2007], where the amplitude of the lift force fluctuations was of the same order of magnitude as the drag force fluctuations. By considering $S^g_{F_1} = S^g_{F_3} = S^g_{F_2}$, we also assume for simplicity that the instantaneous lift and cross-stream coefficients C_L (denoted C_1 in the following) and C_C (denoted C_3 in the following) are equal to the instantaneous drag coefficient C_D defined in equation (2) (denoted C_2 in the following).

Since the force history $F_2(t, \mathbf{x}_0)$ is governed by the instantaneous flow velocity time series $u_2(t, X_1)$ (see equation (2)), we first calculate the PSD $S_{u_2}(f, X_1)$ of $u_2(t, X_1)$ in section 2.1. Then we use $S_{u_2}(f, X_1)$ to calculate the PSD $S^g_{F_2}(f, \mathbf{x}_0)$ in section 2.2. Using $S^g_{F_1} = S^g_{F_3} = S^g_{F_2}$, we calculate the PSD S_{F_i} for all directions. Finally, after having derived the appropriate Green's function $G_{pi}(f, \mathbf{x}; \mathbf{x}_0)$ in section 2.3, we predict the ground power $P^T_{w_p}(f, \mathbf{x})$ by solving equation (7) in section 2.4.

2.1. Flow Velocity Spectrum

In this section, we calculate the PSD S_{u_2} of flow velocity fluctuations in the streamwise direction, upstream of a given grain and in the seismic frequency range 1–100 Hz, since frequency will not change as pressure fluctuations caused by velocity fluctuations are converted into seismic waves.

For simplicity and because of the lack of knowledge about the turbulent flow field within the height of bed roughness above the bed, we assume that the elevation X_1 at which $S_{u_2}(f, X_1)$ operates does not depend on the considered grain diameter D, and we write $S_{u_2}(f, X_1) = S_{u_2}(f, X^r_1)$, where X^r_1 corresponds to a reference elevation within the bed roughness. Here we set $X^r_1 = k_s/2$, where $k_s = 3D_{50}$ [*Kamphuis*, 1974] corresponds to the roughness size (see Figure 1b), D_{50} being the median grain size. Under this rewriting, the velocity spectrum upstream of the different riverbed grains depends on the roughness size but is independent of grain size. The Reynolds decomposition of the instantaneous streamwise velocity $u_2(t, X_1)$ at elevation $0 < X_1 \leq k_s$ above the bed, i.e., within the roughness layer, is introduced by writing $u_2(t, X_1) = \bar{u}_2(X_1) + u'_2(t, X_1)$, where $\bar{u}_2(X_1)$ is the average streamwise velocity and $u'_2(t, X_1)$ is the fluctuating streamwise velocity.

The depth variation of $\bar{u}_2$ in an open channel flow configuration is commonly described by a logarithmic profile [*Schlichting*, 1979]. However, as a result of grain-induced form drag [*Wiberg and Smith*, 1991] and fluid deformation (i.e., eddy viscosity) associated with wakes shed by particles [*Lamb et al.*, 2008b], this logarithmic profile likely only poorly represents the average flow velocities within the bed roughness [*Nikora et al.*, 2001, 2004; *McLean and Nikora*, 2006]. Instead, the average velocity profile therein depends on the relative roughness of the flow [*Bayazit*, 1976; *Tsujimoto*, 1991] defined as the ratio k_s/H, where H is water flow depth (see Figure 1). To describe the average streamwise velocity $\bar{u}_2$ at elevation X_1 within the bed roughness, we use the semiempirical formulation proposed by *Lamb et al.* [2008b]

$$\bar{u}_2(X_1) \approx c_{\bar{u}}(X_1)u_*, \tag{8}$$

where $c_{\bar{u}}(X_1) = \frac{X_1}{0.12k_s}\left(1 - \left(\frac{X_1}{2k_s}\frac{k_s}{H}\right)\right)$ and u_* is the flow shear velocity at the bed.

Turbulence intensity, i.e., the root-mean-square of the fluctuating streamwise velocities $\sigma_{u_2}(X_1) = \sqrt{\overline{u_2'(t,X_1)^2}}$, is also affected by particle roughness. Accordingly, $\sigma_{u_2}(X_1)$ exhibits a maximum value $\sigma_{u_2,\max}$ near the top of the roughness layer, i.e., at $X_1 \approx k_s$ [*Raupach et al.*, 1991; *Nikora and Goring*, 2000; *Nezu and Rodi*, 1986]. The change in σ_{u_2} with decreasing elevation X_1 within the bed roughness is poorly known because turbulent velocity measurements are difficult to conduct there. Thus, we assume that σ_{u_2} does not depend on X_1, and we denote $\sigma_{u_2} = \sigma_{u_2}(X_1) = \sigma_{u_2,\max}$ as well as $u_2'(t) = u_2'(t,X_1)$. Based on laboratory [*Bayazit*, 1976; *Wang et al.*, 1993; *Carollo et al.*, 2005] and field [*Nikora and Goring*, 2000; *Legleiter et al.*, 2007] measurements that report significant variations of $\sigma_{u_2,\max}$ with relative roughness k_s/H, a dependence of σ_{u_2} with k_s/H is introduced following the semiempirical formula derived in *Lamb et al.* [2008b] as

$$\sigma_{u_2} \approx c_\sigma u_*, \tag{9}$$

where $c_\sigma = 0.2\left[5.62\log_{10}\left(\frac{H}{k_s}\right) + 4\right]$.

For river flows, which are characterized by a large Reynolds number $Re = \bar{u}_2(X_1)H/\nu > 10^4$ where ν is the kinematic viscosity of the fluid, kinetic energy inherited from the mean flow is transferred to small scales by means of turbulent eddies [*Tennekes and Lumley*, 1972; *Nezu and Rodi*, 1986; *Venditti et al.*, 2013]. In such open channel flows, turbulent eddies form close to the riverbed from the large shear stress that operate there [*Kline et al.*, 1967; *Nakagawa and Nezu*, 1981; *Roy et al.*, 2004]. We approximate the macroscopic shearing at the origin of eddy formation by the one operating at the reference elevation X_1^r and write the associated production rate $\wp$ of turbulent kinetic energy per unit mass (in units of J s^{-1} kg^{-1}) as

$$\wp\left(X_1^r\right) \equiv -\overline{u_1'(t)u_2'(t)}\Gamma_{12}\left(X_1^r\right), \tag{10}$$

where $\Gamma_{12}\left(X_1^r\right) = \frac{\partial \bar{u}_2(X_1^r)}{\partial X_1}$ is the macroscopic mean rate of strain and $\overline{u_1'(t)u_2'(t)}$ is the Reynolds stress [*Tennekes and Lumley*, 1972]. After having formed, these eddies are ejected above the bed roughness and eventually enlarge by coalescence as they are conveyed downstream by the average flow [*Yalin*, 1992]. This burst-like formation process of these eddies at the bed followed by their coalescent growth occurs within a frequency range commonly referred as the productive range. As these eddies become comparable in size to the flow depth, they eventually break up into smaller eddies through a cascading process that allows energy to transfer down to smaller scales. The frequency range associated with this cascading process is commonly referred as the inertial subrange [*Kolmogorov*, 1941], within which energy is transferred down to a minimum spatial scale (the Kolmogorov microscale) at which the energy can be dissipated through viscous friction. The kinetic energy dissipated (per unit mass) at the Kolmogorov microscale is defined as

$$\epsilon \equiv 2\nu \sum_i \sum_j \overline{\gamma_{ij}\gamma_{ij}}, \tag{11}$$

where $\gamma_{ij} = \frac{\partial u_i'(t)}{\partial X_j}$ is the turbulent rate of strain evaluated along direction j for velocity in direction i [*Tennekes and Lumley*, 1972]. Assuming an idealized steady, homogeneous, and simple shear open channel flow, the rates of turbulent production and dissipation balance [*Tennekes and Lumley*, 1972] so that at elevation X_1^r we have

$$\epsilon\left(X_1^r\right) = \wp\left(X_1^r\right). \tag{12}$$

By approximating the average velocity profile described in equation (8) as linear with depth, the mean rate of strain can be written

$$\Gamma_{12}\left(X_1^r\right) \approx \frac{\bar{u}_2(k_s)}{k_s} \approx c_{\bar{u}}(k_s)\frac{u_*}{k_s}, \tag{13}$$

where $\bar{u}_2(k_s)$ corresponds to the average streamwise velocity at the top of the roughness layer. Moreover, based on previous measurements that report $\overline{u_1'(t)u_2'(t)}/(\sigma_{u_1}\sigma_{u_2}) \approx 0.5$ within the bed roughness [*Nezu and Nakagawa*, 1993], we approximate the Reynolds stress at X_1^r as

$$\overline{u_1'(t)u_2'(t)} = \frac{\sigma_{u_1}\sigma_{u_2}}{2} \approx \frac{(c_\sigma u_*)^2}{2}, \tag{14}$$

where the assumption of isotropic turbulence has been used to approximate $\sigma_{u_1} = \sigma_{u_2} \approx c_\sigma u_*$ using equation (9). Substituting the expressions for the mean rate of strain (equation (13)) and Reynolds stress (equation (14)) into the production rate of equation (10), the turbulent dissipation $\epsilon\left(X_1^r\right)$ operating within the bed roughness can be approximated through equation (12) as

$$\epsilon\left(X_1^r\right) \approx \frac{c_{\bar{u}}(k_s)c_\sigma^2 u_*^3}{2k_s}. \tag{15}$$

The frequency range of the inertial subrange can be shown by substituting the expression of $\epsilon\left(X_1^r\right)$ in equation (15) into its definition in equation (11) and realizing that, given the characteristic Reynolds numbers $Re \sim 10^4$–10^5 encountered in river flow, turbulent dissipation (governed by γ_{ij}) operates at much larger frequencies than turbulent production (governed by Γ_{12}, see equation (13)). Each frequency band lying within these frequency limits corresponds to a single range of eddy sizes. *Kolmogorov* [1941] formalized the energy transfer through the intermediate scales of the inertial subrange, e.g., from the largest eddies to the smallest ones, and derived the famous "−5/3 law" for the energy spectrum. The nonnormalized Kolmogorov spectrum E_{u_2} that defines the power spectrum of the streamwise velocity time series can be described at elevation X_1^r and in wave number space following *Nezu and Nakagawa* [1993] as

$$E_{u_2}\left(k_w, X_1^r\right) = K\epsilon\left(X_1^r\right)^{2/3} k_w^{-5/3}, \tag{16}$$

where $K = 0.5$ is the Kolmogorov universal constant and k_w is the wave number associated with velocity fluctuations at elevation X_1^r within the water layer. By assuming that eddies of all sizes travel at the same downstream average velocity $\bar{u}_2\left(X_1^r\right)$, Taylor's frozen-turbulence hypothesis [*Taylor*, 1938] can be used to convert the PSD $E_{u_2}\left(k_w, X_1^r\right)$ of equation (16) expressed in the wave number space into the PSD $S_{u_2}(f, X_1^r)$ expressed in the frequency domain as

$$\begin{aligned} S_{u_2}(f, X_1^r) &= \frac{2\pi}{\bar{u}_2\left(X_1^r\right)} E_{u_2}\left(k_w, X_1^r\right) = K\left(\frac{2\pi}{\bar{u}_2\left(X_1^r\right)}\right)^{-2/3} \epsilon\left(X_1^r\right)^{2/3} f^{-5/3} \\ &\approx \frac{K}{5} k_s^{-\frac{2}{3}} \left[c_{\bar{u}}\left(X_1^r\right) c_{\bar{u}}(k_s) c_\sigma^2\right]^{\frac{2}{3}} u_*^{8/3} f^{-5/3}, \end{aligned} \tag{17}$$

where $k_w = 2\pi\bar{u}_2\left(X_1^r\right)/f$ has been used and equation (8) for $\bar{u}\left(X_1^r\right)$ and equation (15) for $\epsilon\left(X_1^r\right)$ have been substituted. Equation (17) holds within the inertial subrange, and the predicted −5/3 frequency scaling is an inherent feature of river flows, which has been widely observed in flume experiments and natural rivers [*Nezu and Nakagawa*, 1993]. It is important to note, however, that equation (17) does not incorporate the complex processes that operate within the productive range, where single/clustered burst eddies [*Nikora*, 2011] or large-scale flow structures [*Marquis and Roy*, 2013] form. These large structures, which have sizes that are typically on the order of several flow depths [*Venditti et al.*, 2013], operate at frequencies that are lower than 1 Hz for most rivers, i.e., lower than the frequency range of interest here. As a consequence, these coherent structures are not included in our analysis.

The maximum frequency of the inertial subrange is set by the Kolmogorov microscale η_{Kolmo}. For typical Reynolds numbers associated with river flow, this upper bound frequency is on the order of $f_{\max} \approx \bar{u}_2\left(X_1^r\right)/(2\pi\eta_{\text{Kolmo}}) \approx 10^3$–$10^5$ Hz [*Tennekes and Lumley*, 1972]. As $f_{\max}$ is orders of magnitude larger than the maximum seismic frequency of 10^2 Hz considered here, the tail end of the Kolmogorov energy spectrum does not affect the predictions and is consequently not modeled.

Within the roughness layer, the minimum frequency f_{min} of the inertial subrange is set by the macroscale there (also called the correlation length or mixing length), which we denote l_c [*Tennekes and Lumley*, 1972; *Nezu and Nakagawa*, 1993]. *Nikora et al.* [2001] and *Defina and Bixio* [2005] argue that l_c is dominated by wakes shed by particles within the bed roughness, and thus is set by the roughness scale k_s [*Schlichting*, 1979; *Wiberg and Smith*, 1991; *Lamb et al.*, 2008b]. The minimum frequency therefore scales as the bed shear velocity divided by the roughness scale k_s, or more precisely we have $f_{min} \approx \bar{u}_2\left(X_1^r\right)/(\pi k_s)$ [*Tennekes and Lumley*, 1972]. For the Trisuli and Colorado Rivers and many mountain streams, f_{min} can be estimated to be about 1 Hz.

In the remainder of this paper, f_{min} is the lower bound of the frequency range of interest and we therefore do not include a cutoff at f_{min}. However, for completeness, this truncation could be incorporated as [*Tennekes and Lumley*, 1972]

$$\begin{aligned} S_{u_2}(f, X_1^r) &\approx \tfrac{9}{5} K \left(\tfrac{2\pi}{\bar{u}_2(X_1^r)}\right)^{-2/3} \epsilon \left(X_1^r\right)^{2/3} f_{min}^{-5/3} \cdot \left[1 - \tfrac{5}{11}\left(\tfrac{f}{f_{min}}\right)^2\right] \quad \text{if} \quad f < f_{min} \\ S_{u_2}(f, X_1^r) &\approx K \left(\tfrac{2\pi}{\bar{u}_2(X_1^r)}\right)^{-2/3} \epsilon \left(X_1^r\right)^{2/3} f^{-5/3} \qquad\qquad\qquad\qquad \text{if} \quad f > f_{min}. \end{aligned} \tag{18}$$

Also, one can check that the integral of the Kolmogorov spectrum approaches the total energy of the fluctuating velocities, i.e., that we have

$$\int_{f_{min}}^{f_{max}} S_{u_2}(f, X_1^r) df \approx \sigma_{u_2}^2 \approx (c_\sigma u_*)^2. \tag{19}$$

2.2. Force Spectrum

Here the PSD $S_{F_2}^g$ of the drag force time series acting on a given riverbed grain is calculated from the PSD S_{u_2} of the velocity time series defined previously. As discussed previously, $S_{F_1} = S_{F_3} = S_{F_2}$ is assumed so that all three force components can be included in our analysis. Finally, the PSD S_{F_i} of the force time series per unit length of river and per unit grain size (resulting from the sum of the force time series applied along direction i on each riverbed grain of a given grain size distribution) is calculated by integrating $S_{F_i}^g$ over a unit length of river and a unit grain size.

2.2.1. Calculation of $S_{F_2}^g$

The instantaneous total force applied on a given grain in equation (2) results from the spatial averaging of the instantaneous pressure differentials and shear stresses caused by the turbulent flow on subareas dA of A. We assume that the instantaneous stresses applied over these different subareas are only generated by the instantaneous velocities resulting from the free-stream turbulence and impinging upon the grain. Therefore, we neglect the potential contribution of grain vibrations through vortex shedding and wake flapping [*Achenbach*, 1974; *Sarpkaya*, 1979; *Yuan and Michaelides*, 1992], which would result from velocity fluctuations occurring within the downstream wake of riverbed grains. The incorporation of these turbulent processes related to the dynamics of grain wakes in the model would require distinguishing them from free-stream turbulence. However, such a distinction is a difficult task within the bed roughness, since most of the grains lie within the downstream wake of other grains [*Schmeeckle and Nelson*, 2003]. Moreover, the characteristic scales for structures within the wakes behind particles are likely the same as those for free-stream turbulence in the roughness layer, namely u_* and D. Thus, by using the free-stream turbulent flow field described in the previous section, we assume that the incremental fluctuating force $dF_2(t, X_1^{dA})$ on a subarea dA centered at elevation X_1^{dA} can be described like equation (2) for the instantaneous velocity $u_2(t, X_1^{dA})$ operating over that area. Thus, as done in *Naudascher and Rockwell* [2005], we rewrite equation (2) at the subgrain scale as

$$\frac{dF_2\left(t, X_1^{dA}\right)}{dA} = \frac{C_2 \rho_w}{2}\left[\bar{u}_2\left(X_1^{dA}\right) + u_2'(t, X_1^{dA})\right]^2. \tag{20}$$

By also assuming that the average velocity $\bar{u}_2(X_1^{dA})$ is uniform over A, we approximate its value as $\bar{u}_2(X_1^{dA}) \approx \bar{u}_2\left(X_1^r\right)$ and rewrite equation (20) as

$$\frac{dF_2\left(t, X_1^{dA}\right)}{dA} \approx \frac{C_2 \rho_w}{2} \bar{u}_2\left(X_1^r\right)^2 + C_2 \rho_w \bar{u}_2\left(X_1^r\right) u_2'\left(t, X_1^{dA}\right), \tag{21}$$

where the term of order $\left(u_2'(t, X_1^{dA})/\bar{u}_2\left(X_1^r\right)\right)^2$ has been omitted because the amplitude of $u_2'(t, X_1^{dA})$ is of order $\sigma_{u_2,\max}$, which implies that the ratio $\left(u_2'\left(t, X_1^{dA}\right)/\bar{u}_2\left(X_1^r\right)\right)^2$ is of order $\left[c_\sigma/c_{\bar{u}}\left(X_1^r\right)\right]^2$ (using equations (8)

and (9)). For typical relative roughness values of $H/k_s \approx 1$–10, we obtain $\left(u_2'\left(t, X_1^{dA}\right)/\bar{u}_2\left(X_1^r\right)\right)^2 \sim 10^{-1}$, and the terms of order $\left(u_2'\left(t, X_1^{dA}\right)/\bar{u}_2\left(X_1^r\right)\right)^2$ can thus be neglected. By identifying the terms of the instantaneous force $dF_2(t, X_1^{dA})$ defined in equation (21) into an average force component $d\bar{F}_2\left(X_1^{dA}\right)$ and a fluctuating force component $dF_2'\left(t, X_1^{dA}\right)$, we have

$$\frac{d\bar{F}_2\left(X_1^{dA}\right)}{dA} \approx \frac{C_2\rho_w}{2}\bar{u}_2\left(X_1^r\right)^2 \tag{22a}$$

$$\frac{dF_2'\left(t, X_1^{dA}\right)}{dA} \approx C_2\rho_w\bar{u}_2\left(X_1^r\right)u_2'\left(t, X_1^{dA}\right). \tag{22b}$$

Following *Naudascher and Rockwell* [2005], the mean square contribution of the fluctuating stress time series $\frac{dF_2'\left(t,X_1^{dA^a}\right)}{dA^a}$ and $\frac{dF_2'\left(t,X_1^{dA^b}\right)}{dA^b}$ acting at two different locations a and b of A can be defined in the frequency domain by the cospectral density

$$\Sigma_2^{ab}(f;D) \equiv \frac{\overline{\left[\frac{dF_2'\left(t,X_1^{dA^a}\right)}{dA^a}\frac{dF_2'\left(t,X_1^{dA^b}\right)}{dA^b}\right]_f}}{df}, \tag{23}$$

and the resulting PSD $S_{F_2}^g(f;D)$ applied on A is defined as

$$S_{F_2}^g(f;D) \equiv \int\!\!\int_A \Sigma_2^{ab}(f;D)dA^a dA^b. \tag{24}$$

By using the decomposition of forces formulated in equation (22) to express $\frac{dF_2'\left(t,X_1^{dA^a}\right)}{dA^a}$ and $\frac{dF_2'\left(t,X_1^{dA^b}\right)}{dA^b}$ in equation (23), we can write the cospectral density of stresses as

$$\Sigma_2^{ab}(f) \approx \left(C_2\rho_w\bar{u}_2\left(X_1^r\right)\right)^2 S_{ab}^g(f), \tag{25}$$

where $S_{ab}^g(f) = \frac{\overline{\left[u_2'\left(t,X_1^{dA^a}\right)u_2'\left(t,X_1^{dA^b}\right)\right]_f}}{df}$ is the cospectral density of velocities acting at the two different locations a and b of the grain surface. The power spectral density of forces resulting from the combination of all forces applied on the grain is obtained by substituting equation (25) into the integral formulation of equation (24), which leads to

$$S_{F_2}^g(f;D) \approx \left(C_2\rho_w\bar{u}_2\left(X_1^r\right)A\right)^2\frac{1}{A^2}\int\!\!\int_A S_{ab}^g(f)dA^a dA^b. \tag{26}$$

Finally, following the assumption that $S_{F_1} = S_{F_3} = S_{F_2}$ and substituting the PSD $S_{u_2}(f, X_1^r)$ defined in equation (17) of the previous section into equation (26) through defining the function $\chi_{fl}(f;D)^2 = \frac{1}{A^2}\int\!\!\int_A \frac{S_{ab}^g(f)}{S_{u_2}(f,X_1^r)}dA^a dA^b$, the PSD of force fluctuations obtained in equation (26) along the downstream direction can be rewritten for force fluctuations operating in any direction i as

$$S_{F_i}^g(f;D) \approx \left(C\rho_w\bar{u}_2\left(X_1^r\right)A\right)^2 S_{u_2}(f,X_1^r)\chi_{fl}(f;D)^2, \tag{27}$$

where $C = C_1 = C_3 = C_2$ and S_{u_2} is the PSD of flow velocities obtained in equation (17).

Equation (27) states that the energy of the fluctuating force applied over the entire area A, which results from the summation of all the fluctuating forces applied on the subareas dA, is proportional to the square of the average downstream velocity. In addition, at a given frequency f, the resultant fluctuating force amplitude is lessened by a normalization factor $\chi_{fl}(f;D)^2 \leq 1$, where $\chi_{fl}(f;D)^2$ expresses the capability of a riverbed grain to convert velocity fluctuations into force fluctuations. The larger the eddy size is with respect to the area A, the more similar time variations of $u_2'(t, X_1^{dA^a})$ and $u_2'(t, X_1^{dA^b})$ are, and thus the greater is $S_{ab}^g(f)$. This feature is related to the fluid-dynamic admittance of a given rigid surface, which defines how easily velocity fluctuations operating in the fluid are converted into force fluctuations operating on the solid.

We follow *Naudascher and Rockwell* [2005] and use an empirical formulation based on experimental tests conducted on plates of various geometries to express $\chi_{fl}(f;D)$ as

$$\chi_{fl}(f;D) = \frac{1}{1+\left[\frac{2f}{f_c(D)}\right]^{4/3}}, \tag{28}$$

where $f_c(D) \equiv \bar{u}_2\left(X_1^r\right)/D$ describes a cutoff frequency above which χ_{fl} decreases as a result of local force fluctuations that increasingly cancel each other at increasing frequencies.

2.2.2. Calculation of S_{F_i}

The resultant force applied on the full width and on a unit length of river corresponds to the spatial average of all forces applied on each riverbed grain. In order to sum up all contributions, we assume that the force time series are randomly spaced in time from one grain to another. Such behavior is expected for grain sizes of the order or larger than the bed roughness size k_s where, in that case, the grains are separated by a distance larger than the correlation length $l_c \approx k_s$ considered for the turbulent flow. For smaller grains, the assumption of a random time spacing of force time series from one grain to another is less appropriate, as the turbulent flow velocities are expected to be correlated up to spatial scales that are larger than a single grain size. However, in practice, the turbulent flow field within the bed roughness may be dominated by the downstream wakes of the particles, causing values of l_c to be of the order of the grain diameter D located upstream of the considered grain [*Schmeeckle and Nelson*, 2003]. The incorporation of these spatial variations of l_c in the present model would require assumptions of grain packing geometries within the bed roughness, which would add considerable complexity. Thus, in order to keep the model as simple as possible, we assume the independence of force time series from grain to grain. Under this assumption, the sum of force time series does not affect the shape of the spectrum defined in equation (27) [see *Tsai et al.*, 2012] and the PSD $S_{F_i}(f,\mathbf{x}_0)$ of the resultant force time series can be written as

$$S_{F_i}(f,\mathbf{x}_0;D) = N_g(D)S^g_{F_i}(f,\mathbf{x}_0;D), \tag{29}$$

where $N_g(D)$ is the number of grains per unit length of river and per unit grain size (N_g has units of m^{-2}).

Following *Tsai et al.* [2012], $N_g(D)$ is calculated using the log-"raised cosine" grain size distribution $p(D)$ that is defined per unit grain size (in unit of m^{-1}). The log-raised cosine distribution is analogous to a lognormal distribution except that it includes a cutoff at both large and small D. Assuming grain assemblies that exhibit packing densities of about 70 to 80% at the riverbed, as, for example, obtained by *Schmeeckle* [2014] in assemblies of circular grains generated numerically under river flow conditions, the number of grains of size D for a unit length of river and a unit grain size can be approximated as

$$N_g(D) \approx \frac{p(D)W}{D^2}, \tag{30}$$

where W stands for the river width.

By substituting the expression of the PSD $S^g_{F_i}(f)$ of forces applied on a single grain (equation (27)) and the expression for the number of riverbed grains $N_g(D)$ (equation (30)) into the PSD $S_{F_i}(f,\mathbf{x}_0;D)$ of force time series applied on all grains per unit length and per unit grain size of river (equation (29)), $S_{F_i}(f,\mathbf{x}_0;D)$ can be approximated as

$$S_{F_i}(f,\mathbf{x}_0;D) \approx \frac{3}{5}Wp(D)D^2\rho_w^2 c_{\bar{u}}\left(X_1^r\right)^2 C^2 u_*^2 S_{u_2}\left(f,X_1^r\right)\chi_{fl}(f;D)^2, \tag{31}$$

where equation (8) has been used for the average velocity $\bar{u}_2\left(X_1^r\right)$. By substituting the expression for $S_{u_2}(f,X_1^r)$ obtained in the previous section (see equation (17)) into equation (31), we obtain a final expression for $S_{F_i}(f,\mathbf{x}_0;D)$ as

$$S_{F_i}(f,\mathbf{x}_0;D) \approx \frac{K}{8}\frac{Wp(D)D^2}{k_s^{2/3}}\rho_w^2 C^2\zeta(H/k_s)u_*^{14/3}f^{-5/3}\chi_{fl}(f;D)^2, \tag{32}$$

where the function

$$\zeta(H/k_s) = \left[c_{\bar{u}}(k_s)^{1/3}c_{\bar{u}}\left(X_1^r\right)^{4/3}c_\sigma^{2/3}\right]^2 \tag{33}$$

accounts for the effect of variations in average velocity and turbulent intensity with apparent roughness into variations in the amplitude of S_{F_i}.

2.3. Green's Function

As stated in the beginning of this model section, a single component p of ground motion is potentially affected by all three force fluctuation components. More precisely, the horizontal (direction 2) and lateral (direction 3) components of forces, i.e., the forces that operate along the Earth's surface plane, generate Love waves, while all the three components (i.e., horizontal, lateral, and vertical) of forces generate Rayleigh waves. Assuming that the local topographic slope of the river bank on which the seismic station is deployed is small, the vertical component of the seismic station is only affected by Rayleigh waves. On the other hand, the broad spatial distribution of turbulent flow noise sources operating all along the river implies both horizontal components of the seismic station to be a combination of both Rayleigh and Love waves. In order to avoid accounting for both Rayleigh and Love waves and separating their contributions, we here only focus on the vertical component of the seismometer and we calculate $P^T_{w_1}(f, \mathbf{x}; D)$ from equation (7), where index 1 indicates the vertical direction (see Figure 1). The amplitude of the Green's function components $G_{1i}(f, \mathbf{x}; \mathbf{x}_0)$ for vertical ground motion caused by an impulse force applied in the ith direction can be calculated for the fundamental mode following *Aki and Richards* [2002] as

$$\left|\begin{matrix} G_{11} \\ G_{12} \\ G_{13} \end{matrix}\right| \approx \frac{1}{8 v_c v_u I_1} \begin{pmatrix} r_1(z_F) r_1(z_S) \\ r_1(z_F) r_2(z_S) \cos\varphi \\ r_1(z_F) r_2(z_S) \sin\varphi \end{pmatrix} \sqrt{\frac{2}{\pi k r}} e^{-\pi f r/(v_u Q)} \tag{34}$$

where $k = 2\pi f / v_c$ is the angular wave number of the Rayleigh wave, v_c is the phase velocity, v_u is the group velocity, $r = |\mathbf{x} - \mathbf{x}_0|$ is the source-station distance, φ is the azimuth, Q is the (dimensionless) quality factor, r_1 and r_2 are the vertical and horizontal Rayleigh wave eigenfunctions that describe ground displacement amplitude as a function of depth in the respective directions, z_F and z_S are the depths below ground surface of the point source and the seismic station, respectively, and I_1 is the energy integral of the Rayleigh surface wave defined as

$$I_1 = \frac{1}{2} \int_0^\infty \rho_s(z) (r_1(z)^2 + r_2(z)^2) \mathrm{d}z, \tag{35}$$

where ρ_s is rock density and z denotes depth below ground surface.

It is important to notice at this stage that the term $\sqrt{\frac{2}{\pi k r}}$ in equation (34) approximates Rayleigh wave attenuation from far-field geometrical spreading, i.e., in the spatial domain where the distance between the station and the source (the river) is much larger than the wavelength of the Rayleigh wave. Another approximation for this geometrical spreading is suggested in section 4.2 in order to account for the near-field situation encountered at "Hance Rapids" in the Colorado River (United States).

Since the seismic wavelengths of interest are much larger than the source depth $z_F \approx H$, we write $z_F = z_S \approx 0$ and follow *Tsai and Atiganyanun* [2014] by defining the nondimensional numbers N_{11} and N_{12} as

$$N_{11} = \frac{\rho_s(0) r_1(0) r_1(0)}{k I_1}; \quad N_{12} = \frac{\rho_s(0) r_1(0) r_2(0)}{k I_1}, \tag{36}$$

so that the Green's function expressed in equation (34) reduces to the surface-to-surface Green's function written as

$$\left|\begin{matrix} G_{11} \\ G_{12} \\ G_{13} \end{matrix}\right| = \frac{k}{8 \rho_s(0) v_c v_u} \begin{pmatrix} N_{11} \\ N_{12} \cos\varphi \\ N_{12} \sin\varphi \end{pmatrix} \sqrt{\frac{2}{\pi k r}} e^{-\pi f r/(v_u Q)}. \tag{37}$$

We consider the "generic rock site" defined by *Boore and Joyner* [1997] from seismic investigations conducted at various locations on the continental crust, in which rock density ρ_s empirically scales with shear velocity v_s as $\rho_s = 2500 + 93.75 \cdot (v_s/1\ \mathrm{km/s} - 0.3)$ and shear velocity is described as a function of depth as a piecewise power law. Following the simulation results of *Tsai and Atiganyanun* [2014] performed in this specific configuration, N_{11} and N_{12} can be approximated in the 1 to 10 Hz frequency range (which is the frequency range we mainly focus on below to test our model against observations) as

$$N_{11} \approx 0.6; \quad N_{12} \approx 0.8. \tag{38}$$

These expressions for N_{11} and N_{12} imply a horizontal to vertical ratio, i.e., $r_2(0)/r_1(0)$ ratio, of the order of 1.3, which roughly corresponds to that modeled in the 1 to 10 Hz frequency range in *Bonnefoy-Claudet et al.*

[2006]. Also, from *Tsai and Atiganyanun* [2014], we describe the Rayleigh wave phase and group velocities v_c and v_u as

$$v_c(f) = v_{c0}(f/f_0)^{-\xi}$$
$$v_u(f) = v_c(f)/(1+\xi), \tag{39}$$

where $f_0 = 1$ Hz, $v_{c0} = 2175$ m/s, and $\xi = 0.48$. Finally, following *Erickson and McNamara* [2004], the quality factor Q is modeled in the form of

$$Q = Q_0(f/f_0)^{\eta}, \tag{40}$$

where Q_0 and η are constant parameters. As in *Tsai et al.* [2012] and following the suggestions of *Anderson and Hough* [1984], we consider $Q_0 = 20$ and $\eta = 0$.

2.4. Final Model Formulation

In order to obtain our final model, the average shear velocity at the average bed elevation is written assuming a steady and uniform flow (when averaged over turbulence) as

$$u_* = \sqrt{gH\sin\theta}, \tag{41}$$

where g is the acceleration due to gravity and θ is the channel slope angle. *Schmeeckle et al.* [2007] measured typical values of C_2 (i.e., instantaneous drag coefficient) in flume experiments and reported values increasing from 0.4 to 1.6 as the average streamwise velocity is decreased. For simplicity, we here do not account for a dependence of $C = C_2$ with the average downstream velocity, and we set $C = 0.5$. Since the PSDs of force fluctuations are assumed similar in all directions i, we denote $S_F = S_{F_i}$.

By substituting the expression for the Green's function provided in equation (37) into the expression for the total predicted seismic power recorded at a given station (equation (7)), $P^T_{w_1}(f,\mathbf{x})$ can be approximated as

$$P^T_{w_1}(f,\mathbf{x}) \approx 4\pi^2 f^2 \int_R \left[\int_D S_F(f,\mathbf{x}_0;D)\mathrm{d}D\right]\cdot\left(\frac{k}{8\rho_s(0)v_c v_u}\right)^2 \frac{2}{\pi k r} e^{-2\pi f r/(v_u Q)}\mathrm{d}\mathbf{x}_0. \tag{42}$$

The total PSD of ground motion recorded at $\mathbf{x}$ is obtained by substituting equation (32) for the force spectrum S_F into equation (42). By assuming constant flow conditions along the river and a distance r_0 between the seismic station and the river that is much larger than the width W of the river, we use the definitions of the wave propagation parameters provided in equations (39) and (40) and rewrite equation (42) as

$$P^T_{w_1}(f) \approx \frac{KW}{3k_s^{2/3}}\left(\frac{\rho_w}{\rho_s(0)}\right)^2 \frac{(1+\xi)^2}{f_0^{5\xi}v_{c0}^5}\cdot\zeta(H/k_s)\cdot\psi_\beta(f)\cdot\phi_D(f)\cdot f^{4/3+5\xi}\cdot g^{7/3}\sin(\theta)^{7/3}\cdot C^2H^{7/3} \tag{43}$$

where

$$\begin{cases}\phi_D(f) = \int_D p(D)D^2\chi_{fl}(f;D)^2\mathrm{d}D\\ \psi_\beta(f) = \int_R \frac{1}{r}e^{-2\pi f r/(v_u Q)}\mathrm{d}\mathbf{x}_0.\end{cases} \tag{44}$$

Function $\phi_D(f)$ represents the modulation of the predicted ground velocity PSD by grain sizes, while function $\psi_\beta(f)$ accounts for geometrical spreading and inelastic attenuation of seismic waves as they propagate into the ground. As in *Tsai et al.* [2012], $\psi_\beta(f)$ can be approximated analytically by assuming an infinitely long and straight river whose closest point in the horizontal Earth's surface plane is r_0 from the seismic station and writing

$$\psi_\beta(f) = \int_{-\infty}^{\infty}\frac{1}{\sqrt{1+y^2}}\exp\left(-\beta\sqrt{1+y^2}\right)\mathrm{d}y \approx 2\log\left(1+\frac{1}{\beta}\right)e^{-2\beta} + (1-e^{-\beta})e^{-\beta}\sqrt{\frac{2\pi}{\beta}}, \tag{45}$$

where

$$\beta = 2\pi r_0(1+\xi)f^{1+\xi-\eta}/\left(v_{c0}Q_0 f_0^{\xi-\eta}\right). \tag{46}$$

It is shown in the application of our model calculations to the observations of *Schmandt et al.* [2013] at Hance Rapids that the infinitely long river hypothesis and the infinitely thin approximation used here to integrate the noise sources are not appropriate, as the rapids section is relatively short and the river-to-station

Table 1. Default Parameters Used to Perform Model Predictions at the Trisuli River and Hance Rapids

	Trisuli River	Hance Rapids
Seismic Parameters		
v_{c0} (m/s)	2175	2175
ξ	0.48	0.48
z_0	1000	1000
η	0	0
Q_0	20	9
r_0 (m)	600	varies with transect from 37.5 to 122.5
f_0 (Hz)	1	1
River Geometry		
θ	1.4°	1.15°
W (m)	50	90
H (m)	4	1.64–4.14 (see Figure 10c)
D_{50} (m)	0.15	0.5
σ_g	0.52	0.7

distance is about the river width. As a consequence, we present in section 4.2 another way of integrating equation (42) that accounts for this complexity.

The strong scaling of $P^T_{w_1}$ with H (to the 7/3 power) in equation (43) shows that seismic observations are strongly set by water flow depth. This also implies a strong scaling with u_* (see equation (41)), such that seismic observations ($P^T_{w_1}$) may be used to invert for u_* and H. A quantitative evaluation of the model is performed in section 4 against the observations reported by *Schmandt et al.* [2013] in the Colorado River, United States. Prior to this, the role of model parameters and their associated uncertainties in model predictions (equation (43)) is explored in section 3.

3. Model Features

Here we provide a general view on the behavior of model predictions with varying model parameters. Moreover, the turbulent flow model predictions are compared with those for a bedload source using the model of *Tsai et al.* [2012], who derived the PSD $P^T_{b_1}$ of vertical ground velocities resulting from a sediment flux q_b transported as bedload. It is important to note that, in this comparison, similar granulometries are considered between grains transported as bedload and grains that form the roughness layer. In reality, the riverbed grains transported as bedload can possibly be smaller than the ones forming the roughness layer. Thus, the case considered here corresponds to an end-member configuration where the relative contribution of bedload-induced versus turbulent flow-induced noise evaluated for a given sediment flux q_b and a given flow configuration is maximal, since at constant q_b we expect larger bedload-induced noise for larger grains [see *Tsai et al.*, 2012]. Similar to *Tsai et al.* [2012], we initially apply our model predictions to the Trisuli River, for which *Burtin et al.* [2008] reported seismic noise. The river geometry is described using the same parameters as used in *Tsai et al.* [2012]: we use $W = 50$ m for channel width, $\theta = 1.4°$ for river slope angle, $D_{50} = 0.15$ m for the median size of riverbed grains, and $\sigma_g = 0.52$, where σ_g is the standard deviation of the log-raised cosine distribution $p(D)$ of riverbed grains. Numerical simulations performed recently by *Tsai and Atiganyanun* [2014] provide a more realistic description of the Rayleigh wave propagation compared to the approximations of *Tsai et al.* [2012]; and thus, the seismic wave parameters used here slightly differ from *Tsai et al.* [2012]. Phase and group velocities v_c and v_u are calculated using $v_{c0} = 2175$ m/s and $\xi = 0.48$ in equation (39) (instead of the values of $v_{c0} = 1295$ m/s and $\xi = 0.374$ used in *Tsai et al.* [2012]), and the prefactor N_{11} used in equation (37) is set to 0.6, instead of the value of 1 used by *Tsai et al.* [2012]. We describe the quality factor Q_0 (which quantifies inelastic attenuation) as in *Tsai et al.* [2012], i.e., we use $Q_0 = 20$, $f_0 = 1$ Hz, and $\eta = 0$ in equation (40), and set the river-to-station distance to $r_0 = 600$ m so that it roughly corresponds to the seismic deployments considered by *Burtin et al.* [2008]. Finally, we take $H = 4$ m as water flow depth, as well as $q_b = 0.045$ m^2/s for the bedload flux. This value of q_b is within the range of values inferred by *Tsai et al.* [2012]. These default parameters are listed in Table 1. Ultimately, we provide uncertainty estimates (see section 3.4) for the predictions caused by our imperfect knowledge of both the physics described and the parameter values used in our model.

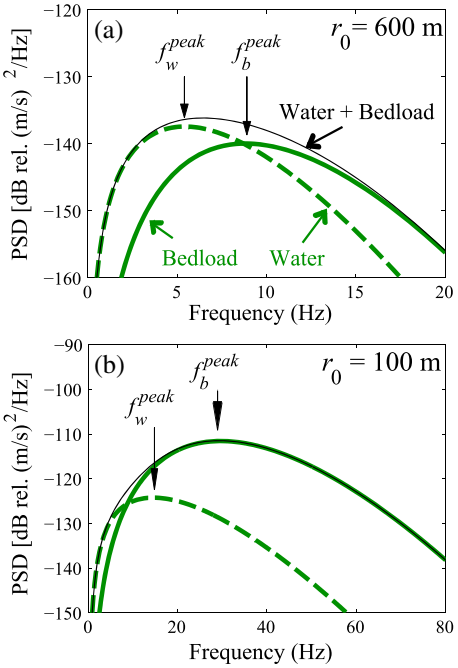

Figure 2. Modeled PSDs resulting from the turbulent flow source (dashed thick green) and the bedload source presented in *Tsai et al.* [2012] (continuous thick green). Using (a) r_0 = 600 m and (b) r_0 = 100 m. Note that different scales have been used for axis between Figures 2a and 2b. Figures 2a and 2b both use the default Trisuli River parameters (see main text), with H = 4 m and q_b = 0.045 m^2/s, where q_b is within the range of values inferred by *Tsai et al.* [2012]. The thin black line indicates the sum of the two model predictions. The frequencies f_w^{peak} and f_b^{peak} correspond to the frequencies at which $P_{w_1}^T$ and $P_{b_1}^T$ (respectively) have their largest values.

3.1. Predictions for the Trisuli River Using Default Model Parameters

Turbulent flow and bedload model PSDs are shown as a function of frequency in Figure 2a using the default Trisuli parameters listed in Table 1. The maximum ground power obtained without tuning any model parameters from the turbulent flow noise model corresponds to −137.4 dB, which is of the same order of magnitude as the maximum PSDs reported in *Burtin et al.* [2008]. Thus, our model predicts that turbulent flow plays a significant role in the PSDs reported by *Burtin et al.* [2008]. In addition, while accounting for turbulent flow noise introduces larger energy at lower frequencies in the total PSDs as compared to the PSD modeled by *Tsai et al.* [2012], the combination of our model with the bedload model of *Tsai et al.* [2012] remains consistent with the general aspects of the observations reported by *Burtin et al.* [2008]. A single peak occurs around ≈6–7 Hz, with energy increasing sharply at low frequencies, in contrast to the gradual decrease at high frequencies. The similarities between the turbulent flow and bedload predictions shown here (along with the known large-bedload signal) explain the difficulties encountered by *Burtin et al.* [2008] in extracting a clear water flow-induced signal from the observed PSDs. These model predictions suggest that the hysteresis curve reported over the broad 3–15 Hz frequency range by *Burtin et al.* [2008] may not solely include bedload, since its shape is expected to largely be influenced by turbulent flow-induced noise. In particular, since the two different sources of noise add with each other, hysteresis is expected to be more pronounced in cases where bedload-induced noise is larger than turbulent flow-induced noise. As bedload-induced noise is predicted to be larger than turbulent flow-induced noise at larger frequencies (see Figure 2a), we expect a more pronounced hysteresis there. We have verified this by taking the raw data at station H0460 (reported in *Burtin et al.* [2008] and available at www.iris.edu) and recalculating the hysteresis curve with respect to water flow depth within the frequency ranges 3–8 Hz and 10–18 Hz (see Figure 3). In agreement with model predictions at station H0460 (see Figure 2a), the hysteresis is more pronounced in the higher-frequency range where bedload-induced noise is predicted to be dominant. While smaller, the observed hysteresis does not completely disappear in the low-frequency range (see blue curve in Figure 3), which is also consistent with our model predictions. Even though turbulent flow-induced noise dominates in the 3–10 Hz frequency range, variations of bedload-induced noise still occur within an order of magnitude (about 10 dB, see Figure 2a) from the turbulent flow-induced noise, and thus still affect the resultant total noise. In that regard, it is interesting to note that the amplitude difference in the rising versus falling limb of the two observed hysteresis curves roughly corresponds to the difference between the predicted total noise power and the predicted water flow-induced noise power.

The relative contribution of turbulent flow versus bedload in the total PSD is, however, predicted to be drastically modified when varying the distance r_0 between the seismic station and the channel. Using r_0 = 100 m as an example (see Figure 2b), the bedload-induced noise dominates most frequencies, while the peak frequencies f_w^{peak} and f_b^{peak} associated with maximum turbulent flow and bedload model PSDs are much larger and more separated from each other.

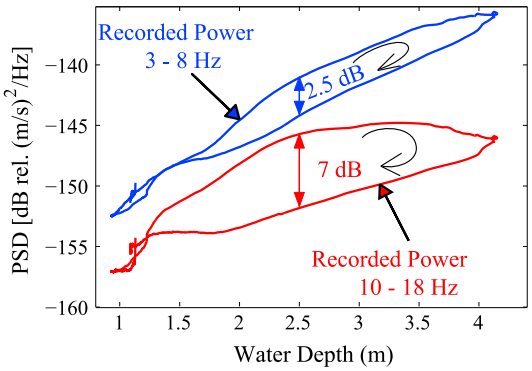

Figure 3. Hysteresis behavior observed during year 2003 and at station H0460 situated about 600 m away from the Trisuli river. Continuous lines correspond to the observed ground velocity power averaged between 3 Hz and 8 Hz (blue) and between 10 Hz and 18 Hz (red). Average observed PSDs and flow depth values have been smoothed at a monthly timescale. The black arrows indicate increasing time of the year.

The following sections discuss in detail the role of model parameters in modifying f_w^{peak} and $P_{w_1}^T\left(f_w^{peak}\right)$, in particular with respect to f_b^{peak} and $P_{b_1}^T\left(f_b^{peak}\right)$.

3.2. Sensitivity of the Peak Frequency on Model Parameters

The functions $\psi_\beta(f)$ and $\phi_D(f)$ of equation (43) are major controls on the predicted frequency scaling with model parameters. $\psi_\beta(f)$ accounts for the modulation of the source spectrum as surface waves travel into the ground, which is set by the river-to-station distance r_0 and the value of the quality factor Q_0 (for a given depth profile of ground shear wave velocities). The surface wave path effect accounted for by $\psi_\beta(f)$ is similar to that of *Tsai et al.* [2012] in the bedload model. As the attenuation of Rayleigh waves preferentially damps larger frequencies (see also equation (37)), f_w^{peak} is predicted to decrease as r_0 increases or Q_0 decreases (see Figures 2 and 4a). Superimposed on this wave path effect, $\phi_D(f)$ modifies the values of f_w^{peak} as turbulent flow velocities are converted into force fluctuations at riverbed grains. For each of the riverbed grains of diameter D, the scaling with frequency of the force spectrum (see equations (27) and (28)) corresponds to the −5/3 Kolmogorov scaling with frequency inherited from the turbulent flow velocities (see equation (17)) on top of which a −8/3 slope decrease is added at frequencies larger than $f_c = \bar{u}_2\left(X_1^r\right)/D$. For a given river slope and a given bed grain size distribution, the value of f_c at which this modification occurs only depends on the riverbed roughness H/k_s (see equation (8)). The larger the ratio H/k_s, the larger the cutoff frequency of χ_{fl}, and thus the larger f_w^{peak} is (see Figure 4a). However, for a given site at which H/k_s values typically vary from a factor of 2 to 4, the changes predicted in f_w^{peak} values are weak. This weak dependence of f_w^{peak} on H/k_s is in agreement with previous observations [*Burtin et al.*, 2008; *Schmandt et al.*, 2013], which report no significant shift in central frequency with varying water discharge.

Note that, in this Trisuli River setting, only flow configurations with values of H/k_s smaller than 32 are considered. Our model is not expected to apply for larger values of H/k_s because grains are transported as suspension for these cases, i.e., from using the default Trisuli parameters with $H = 4$ m the condition $w_s < u_*$

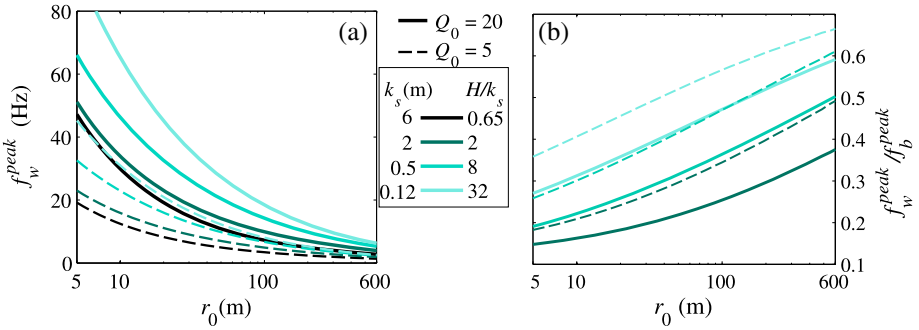

Figure 4. Turbulent flow and bedload peak frequencies variation as a function of source-station distance r_0 with varying roughness size k_s and quality factor Q_0. (a) f_w^{peak} versus r_0. (b) f_w^{peak}/f_b^{peak} versus r_0. Using the default Trisuli River parameters (see main text, H is kept constant and equal to 4 m) except that $D_{50} = k_s/3$ gradually varies from 0.041 m (green line) to 2 m (blue line). As Q_0 may exhibit significant variability from site to site, and is most likely smaller than 20 in those cases [*Schmandt et al.*, 2013], Figure 4 also includes predictions performed using $Q_0 = 5$ (thin dashed lines), in addition to the $Q_0 = 20$ considered in *Tsai et al.* [2012] (thick continuous lines). Note that there are missing curves for $H/k_s = 0.65$ in Figure 4b, since no bedload transport is predicted for this configuration (see equation (47)).

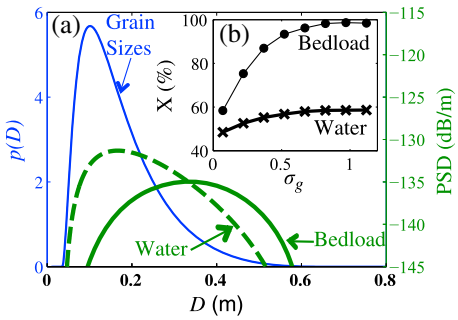

Figure 5. $P^T_{w_1}(f^{peak}_w; D)$ and $P^T_{b_1}\left(f^{peak}_b; D\right)$ resulting from the grain size distribution. (a) Log-raised cosine grain size probability distribution (thin blue, same as *Tsai et al.* [2012]) and resulting PSDs for turbulent flow (thick dashed green) and bedload (thick continuous green, using $q_b = 0.045$ m^2/s) [*Tsai et al.*, 2012]. (b) Grain size percentile X where the grain diameter D_X yields the largest PSD, as a function of the standard deviation of grain sizes σ_g for a turbulent flow (crosses) and bedload (circles) source. Figures 5a and 5b both use the default Trisuli River parameters (see main text).

is reached for most grains when $D_{50} < 0.041$ m ($H/k_s > 32$), where w_s is the settling velocity calculated using the formulation of *Ferguson and Church* [2004].

To compare variations of f^{peak}_w with f^{peak}_b, we approximate f^{peak}_b analytically from *Tsai et al.* [2012] as $f^{peak}_b \approx [4.9Q_0 v_{c0}(1+\xi)f_0^{0.4}/(2.8\pi r_0)]^{1/1.4}$. In agreement with previous observations [*Burtin et al.*, 2011; *Schmandt et al.*, 2013], the negative scaling of the turbulent flow noise with frequency (while the bedload source is constant) causes f^{peak}_w/f^{peak}_b to be consistently lower than 1 (independent of H/k_s and r_0, see Figure 4b), i.e., the water flow-induced noise is predicted to always exist at lower frequencies than the bedload-induced noise. In addition, smaller inelastic attenuation of surface waves, i.e., either smaller values of r_0 or larger values of Q_0, causes the higher-frequency part of the source spectrum to more strongly contribute to the ground velocity PSD. Because the turbulent flow spectrum shows a larger decrease with frequency at these higher frequencies, a slower decrease of f^{peak}_w as compared to f^{peak}_b occurs as r_0 increases or Q_0 decreases, implying that f^{peak}_w/f^{peak}_b increases as r_0 increases or Q_0 decreases, i.e., the frequency range of turbulent flow-induced noise differs less than the one of bedload as r_0 increases or Q_0 decreases. This explains why *Burtin et al.* [2011] and *Schmandt et al.* [2013] could isolate the seismic signature of water flow noise with seismic stations close to the river (e.g., values of $r_0 \approx 10$–50 m have typically been considered in these studies), whereas studies with more distant stations [e.g., *Burtin et al.*, 2008] could not easily do so.

3.3. Sensitivity of PSD Amplitude on Model Parameters

Here the amplitude of model PSDs (see equation (43)) is discussed as a function of grain diameter D (through ϕ_D), roughness of the flow H/k_s (through ζ), river-to-station distance r_0 and ground quality factor Q_0 (through ψ_β), river slope angle θ, and flow depth H.

The amplitude of model predictions resulting from the grain size distribution is shown in Figure 5, in which $P_{w_1}(f^{peak}_w; D)$ is compared with $P_{b_1}\left(f^{peak}_b; D\right)$, where $P_{x_1}\left(f^{peak}_x; D\right)$ (x either stands for w or b) is defined such that $P^T_{x_1}(f) = \int_D P_{x_1}(f; D)\mathrm{d}D$. The peak noise is predicted at $D = 0.18$ m (corresponding to D_{58}, i.e., the 58th percentile grain size) for the turbulent flow model, occurring at a much smaller grain size than the grain size of the maximum $P^T_{b_1}\left(f^{peak}_b; D\right)$ (corresponding to D_{94}) [*Tsai et al.*, 2012]. This difference is due to model predictions that depend on D^2 for turbulent flow (see equation (44)) because larger grains have larger areas exposed to the flow, while they depend on D^6 for bedload because seismic power scales with the mass of impacting grains to the square [*Tsai et al.*, 2012]. Even though the dominant grain size for turbulent flow-induced noise is slightly affected by variations in the standard deviation σ_g of the grain size distribution, it is always larger than the median grain size D_{50} (see Figure 5b) and remains significantly smaller than that which dominates bedload seismic noise. Thus, as compared to the bedload model predictions, accurate knowledge of the tail end of the grain size distribution is less critical in obtaining realistic estimates of the noise caused by turbulent flow. For example, a lognormal distribution could be used instead of the log-raised cosine function used here, which was originally introduced by *Tsai et al.* [2012] to avoid the disproportional and unrealistic contribution of large grains when transported as bedload. For a median grain size of $D_{50} = 0.15$ m, we see in Figure 5 that turbulent flow-induced noise integrated over the whole grain size distribution is about that of the bedload-induced noise. Modification of this picture for varying median grain sizes D_{50}, i.e., roughness scale k_s, is shown at constant water flow depth $H = 4$ m and as a function of r_0 in Figure 6.

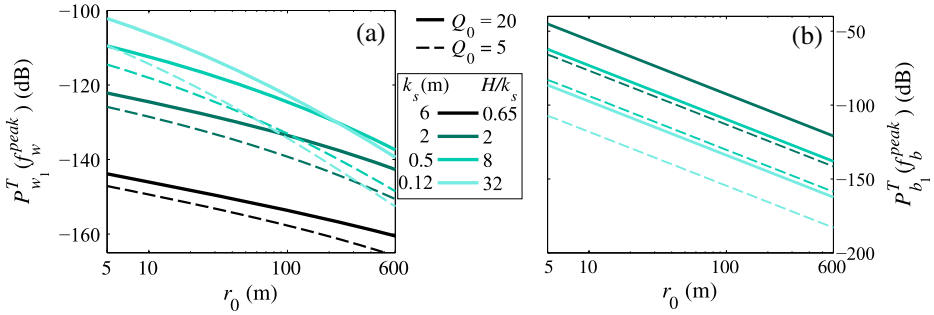

Figure 6. Turbulent flow-induced and bedload-induced maximum seismic power as a function of source-station distance r_0 with varying roughness size k_s. (a) $P^T_{w_1}(f^{peak}_w)$ versus r_0. (b) $P^T_{b_1}(f^{peak}_b)$ versus r_0. Note that different scales have been used for vertical axis between Figures 6a and 6b. Using the default Trisuli River parameters (see main text, H is kept constant and equal to 4 m) except that $D_{50} = k_s/3$ gradually varies from 0.041 m (light green line) to 2 m (dark blue line) and $q_b = q_{bc}/5$, where q_{bc} corresponds to the flux of sediments transported as bedload at transport capacity (see equation (47)). The choice of $q_b = q_{bc}/5$ allows us to account for the expected variations of q_b with D_{50}, while obtaining $q_b \approx 0.045$ m^2/s for the default Trisuli configuration, i.e., for $D_{50} = 0.15$ m. As Q_0 may exhibit significant variations from site to site, and is most likely smaller than 20 in those cases [*Schmandt et al.*, 2013], Figure 6 also includes predictions performed using $Q_0 = 5$ (thin dashed lines), in addition to the $Q_0 = 20$ considered in *Tsai et al.* [2012] (thick continuous lines). Note that there are missing curves for $H/k_s = 0.65$ in Figure 6b, since no bedload transport is predicted for this configuration (see equation (47)).

The turbulent flow-induced noise is compared with that of bedload for a range of median grain sizes D_{50} by calculating $P_{b_1}\left(f_b^{\text{peak}}; D\right)$ using a bedload flux q_b that is scaled with bedload flux at transport capacity q_{bc}, where q_{bc} is calculated following *Fernandez Luque and Van Beek* [1976] as

$$q_{bc} = 5.7\sqrt{RgD_{50}^3}(\tau_* - \tau_{*c})^{3/2}, \tag{47}$$

where $R = 1.8$ is the submerged density, $\tau_* \equiv u_*^2/(RgD)$ is the nondimensional bed stress or Shields stress, and $\tau_{*c} = \tau_{*c50}(D/D_{50})^{-\alpha}$ is the critical value of Shields stress, τ_{*c50} being the critical value of Shields stress for grain size D_{50} and α a constant [*Parker*, 1990]. We consider near equal threshold stress for transport by using $\alpha = 0.9$, which is appropriate for many gravel-bed rivers [*Parker*, 1990] but may be smaller for steep river streams [*Scheingross et al.*, 2013]. We calculate τ_{*c50} from equation (25) of *Lamb et al.* [2008b], which includes the expected dependence of τ_{*c50} on river slope. In contrast to the bedload source, where smaller values of D_{50} cause lower seismic noise as a result of each grain impact having less energy (see Figure 6b), the increasing average and turbulent flow velocities for smaller D_{50} (see equations (8) and (9)) result in larger turbulent flow-induced noise (as shown in Figure 6a at small values of r_0). However, for larger r_0 and/or smaller Q_0, this picture is modified by wave propagation effects. Far away from the river channel, e.g., $r_0 = 600$ m, $P^T_{w_1}$ has the unintuitive behavior of approximately constant $P^T_{w_1}$ with increasing H/k_s values for deep flows. This behavior is explained by the fact that, for strong Rayleigh wave attenuation (either from lower Q_0 or larger r_0), the low-frequency content of the source PSD S_F contributes more to the maximum value of $P^T_{w_1}$ predicted. Because of the less drastic decrease of S_F with frequency in this lower frequency range ($f < f_c$ for most grains in that case, see equation (32) and the associated χ_{fl}-dependence), $P^T_{w_1}$ decreases faster with r_0, and can become lower for deep flows than shallow flows for large enough r_0. Such an unintuitive behavior is not observed for bedload, since the impact contact time is assumed to be smaller than the sampling time of interest, which causes the bedload source spectrum to be frequency independent [*Tsai et al.*, 2012]. Finally, because the PSD S_F decreases with frequency while the bedload source does not, the migration of the signal toward lower frequencies at increasing distance from the river causes a faster decrease of the amplitude of bedload-induced noise with respect to turbulent flow-induced noise.

The different variations of $P^T_{w_1}$ and $P^T_{b_1}$ with r_0, H/k_s, and Q_0 imply that the relative contribution of seismic noise induced by turbulent flow versus seismic noise induced by bedload varies drastically for different flows and seismic deployment configurations (see Figure 7). Obviously, for flow configurations for which no bedload is predicted, the seismic signal is expected to be dominated by turbulent flow-induced noise. When bedload occurs, assuming that the bedload flux evolves in proportion to bedload transport capacity and disregarding cases where a significant portion of grains are expected to be transported as suspension,

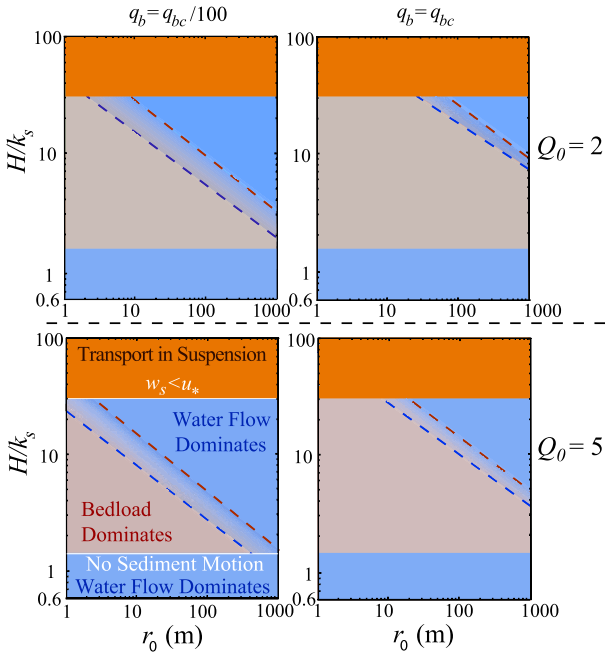

Figure 7. Phase diagrams showing the primary mechanism (i.e., either water flow or bedload) generating peak seismic noise within 1–100 Hz at a given station as a function of its distance from the river and the apparent roughness of the flow. Using the default Trisuli River parameters (see main text, H is kept constant and equal to 4 m) except that $D_{50} = k_s/3$ has been varied from 0.013 m ($H/k_s = 100$) to 2 m ($H/k_s = 0.65$). Left diagrams calculate $P^T_{b_1}$ using $q_b = q_{bc}/100$, while right diagrams use $q_b = q_{bc}$, where q_{bc} is defined in equation (47). Top diagrams have been calculated using $Q_0 = 20$, while $Q_0 = 5$ has been used for bottom diagrams. Blue dashed lines indicate the parameter values where $P^T_{w_1}(f^{peak}_w) = P^T_{b_1}(f^{peak}_w)$, and brown dashed lines indicate the parameter values where $P^T_{w_1}(f^{peak}_b) = P^T_{b_1}(f^{peak}_b)$. The light blue region corresponds to $P^T_{w_1}(f^{peak}_w) > P^T_{b_1}(f^{peak}_w)$ (i.e., turbulent flow-induced noise dominates in its frequency range), while the gray region corresponds to $P^T_{b_1}(f^{peak}_b) > P^T_{w_1}(f^{peak}_b)$ (i.e., bedload-induced noise dominates in its frequency range). There exists a narrow range (between dashed lines) for which both turbulent flow-induced and bedload-induced noise dominate in their respective frequency range. These two regions are bounded by a region of values of H/k_s lower than about 1.3 (in light blue) for which equation (47) predicts no bedload transport and thus water flow-induced noise dominates, and a region of values of H/k_s larger than 32 (in brown), for which we do not expect our model to apply since riverbed grains are in that case transported as suspension, i.e., we have $w_s < u_*$ [*Ferguson and Church*, 2004].

the seismic noise signal is dominated by turbulent flow at large river-to-station distances and large values of H/k_s, while bedload dominates for seismic noise recorded closer to the seismic station and for smaller H/k_s values. Notably, for a given site (i.e., given values of H/k_s and given ground seismic properties), turbulent flow and bedload can be characterized independently by evaluating seismic noise at various distances from the river. There also exists a relatively narrow range of H/k_s and r_0 for which both turbulent flow and bedload exhibit significant amplitudes and different enough frequency ranges such that they can be distinguished from a single record (range delimited by the dashed lines in Figure 7, see section 4 for such a configuration in the case of the Hance Rapids section at the Colorado River).

In this range where turbulent flow-induced noise can be isolated from the seismic signal (shown by the blue areas in Figure 7), the modeling framework presented allows one to invert for water flow depth H directly from equation (43) or for bed shear velocity u_* through equation (41). The direct scaling of ground power resulting from turbulent flow-induced noise with shear velocity u_* or water flow depth H ensures that good constraints can be obtained on these parameters from seismic data, as long as ground motion is evaluated far enough from the river (see Figure 8). When evaluating ground motion closer to the river channel, one needs larger values of u_* in order to be able to distinguish the turbulent flow signature from the bedload signature and thus invert for u_* or H.

The position at which these transitions between turbulent flow and bedload dominated noise occur (i.e., position of the dashed lines in Figures 7 and 8) is also modified by the riverbed slope angle θ. Assuming that bedload transport evolves in proportion to transport capacity for different θ, Figure 9a shows that bedload-induced noise dominates at lower slopes. In contrast, the stronger increase of turbulent flow-induced noise with increasing river slope angle θ results in predominantly turbulent flow-induced noise at steeper slopes. Thus, steeper slopes would cause the dashed lines of Figures 7 and 8 to shift toward the left side of the diagrams, i.e., toward smaller values of r_0. Thus, a larger range of u_* or H-values can be inverted for in these steeper cases.

Finally, to identify the turbulent flow-induced noise signature in seismic data or invert for u_* or H, Figure 9b shows the differential increase of $P^T_{w_1}$ with increasing H. This increase is predicted to be larger for smaller initial H_0/k_s, where H_0 stands for a reference depth. In other words, a similar increase in H results in a larger

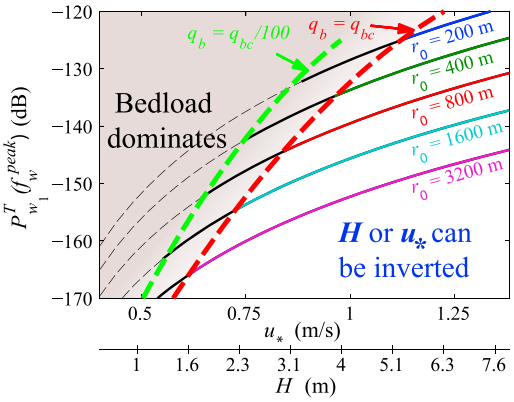

Figure 8. Maximum seismic power $P^T_{w_1}(f^{peak}_w)$ caused by turbulent flow as a function of shear velocity u_* or flow depth H for various distances r_0 from the river. Using the default Trisuli River parameters (see main text) except that H is varied from 0.5 m to 8 m, and various values of r_0 ranging from 200 m (blue line) to 3200 m (purple line) are selected. The dashed red and green lines indicate where the amplitude of bedload-induced noise is similar to the amplitude of turbulent flow-induced noise, i.e., $P^T_{w_1}(f^{peak}_w) = P^T_{b_1}(f^{peak}_w)$. The red dashed line uses $q_b = q_{bc}$ to calculate $P^T_{b_1}(f^{peak}_w)$, while the green dashed line uses $q_b = q_{bc}/100$. The domain lying to the right of the respective dashed lines (unshaded) corresponds to the domain where shear velocity at the bed (or water flow depth) can be inverted from seismic data.

increase in $P^T_{w_1}$ for shallow compared to deeper river flows. It is interesting to note that, over the course of bedload transport evolving in proportion to transport capacity, bedload-induced noise increases considerably slower with H as compared to turbulent flow-induced noise.

3.4. Uncertainties on Model Predictions

Due to our incomplete understanding of some of the physical mechanisms studied and imperfect knowledge of model parameter values, a number of assumptions and approximations have been made. Here we provide a brief discussion of the uncertainties expected of our predictions. Four specific components that we address are the influence of reduced grain exposure to turbulence intensity, nonuniform channel geometry, correlated force fluctuations in the different spatial directions, and specific ground seismic properties of river sites.

For significantly reduced grain exposure (e.g., 50 to 80%) of grains smaller than D_{50} (e.g., reduced turbulence intensity at their lower elevation or flow obstruction from surrounding bigger grains), only minor changes are expected in seismic power amplitude (about 1 dB), since seismic noise from water is dominated by the coarse end of the grain size distribution as a result of a larger area exposed by larger grains to the flow (see Figure 5).

For typical sites, the effect of not accounted changes in river geometry (e.g., channel curvature, nonuniform slope and flow depth) is only significant if they occur within a maximum distance from the seismic station that is about 10 times the river-to-station distance. Under strong river geometry changes within that region, order of magnitude uncertainty is expected on the predicted PSD amplitude (see section 3.3), while a factor of 1.5 uncertainty is expected on the peak frequency (see section 3.2). As examples, these uncertainty levels are reached if one does not account for a large river bend that brings the river 3 times closer to the seismic station, or if one misrepresents local flow depth or river slope by a factor of 2.

For time series of fluid forces on riverbed grains that would be entirely correlated with each other along the three spatial directions, as opposed to entirely uncorrelated as presently assumed, model predictions amplitudes would be increased by a factor of 3, i.e., 4.8 dB (see equations (5) and (6)). Also, even in the extreme scenario where the degree of correlation between the different forces applied on the different directions varies from entirely correlated to entirely uncorrelated over the frequency range of interest, we expect the predicted scaling of ground velocity PSDs with frequency to not be insignificantly modified, since model predictions will only be multiplied by $f^{\pm 0.5}$ as compared to the $f^{3.5}$ scaling predicted (see equation (43)).

For the particular ground settings near the river, which often have thin layers of alluvium overlying hard bedrock, we expect an uncertainty of a factor of about 1.5 for surface wave velocities and a factor of about 2 for the ground quality factor Q (see equation (34)). Within the relatively low frequency range of 1 to 10 Hz in which water flow-induced noise is predicted at both the Trisuli (see section 3.1) and Colorado (see section 4) Rivers, this level of uncertainty leads to order of magnitude uncertainty ($\approx$ 10 dB) on model predictions (see equations (45) and (46)).

Overall, we therefore expect our model predictions to be accurate within an order of magnitude ($\approx$ 10 dB). This order of magnitude uncertainty is mostly due to uncertainties on ground seismic properties and river geometry, which thus would benefit from being constrained independently from targeted measurements. However, we note that the uncertainties here evaluated are absolute uncertainties, and thus do not apply when comparing time relative changes in turbulent flow-induced noise at a given site, in which case we

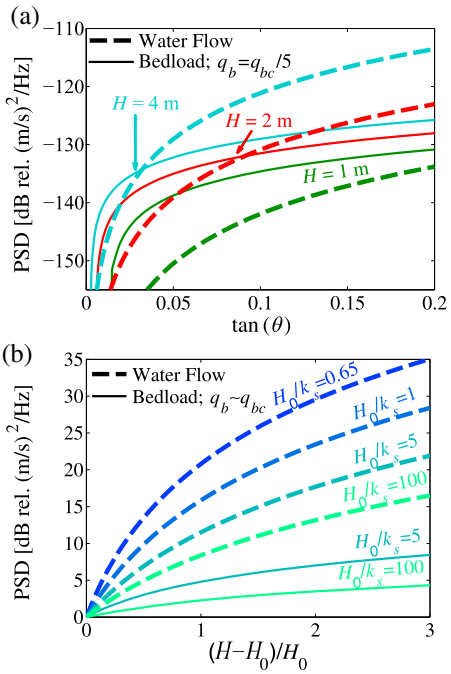

Figure 9. Variations in turbulent flow-induced and bedload-induced seismic noise with variations in river slope and flow depth. (a) $P^T_{w_1}(f^{peak}_w)$ (dashed lines) and $\Delta P^T_{b_1}(f^{peak}_b)$ (continuous lines) versus slope tan(θ) and (b) $\Delta P^T_{w_1}(f^{peak}_w)$ and $\Delta P^T_{b_1}(f^{peak}_b)$ versus normalized depth variation $(H - H_0)/H_0$, where H_0 stands for a reference, initial, water flow depth. Here Δ indicates that a PSD difference is evaluated, i.e., all data points of Figure 9b have been normalized by the PSD calculated at H_0. Figures 9a and 9b both use the default Trisuli River parameters except that both H and θ are varied in Figure 9a, while k_s, θ, H, and H_0 are varied in Figure 9b. As modeled PSDs in Figure 9b are normalized by PSDs obtained at H_0 and k_s, the results do not depend on the absolute values of H_0 and k_s, and also do not depend on the constant used to scale q_b with q_{bc}.

expect good accuracy in model predictions since changes in ground properties and river geometry with time are limited.

4. Model Application to Hance Rapids (Colorado River, United States)

In this section, we quantitatively compare our model predictions to the field seismic observations reported at Hance Rapids (HR) in the Colorado River [*Schmandt et al.*, 2013]. We judge that, to date, only the HR data set provides a clearly separated seismic signature of turbulent flow noise and sufficient information on river geometry and hydrological parameters to make a meaningful model comparison. For other data sets, either a water flow-induced signal has not been clearly identified by the authors, as for the Trisuli (Himalaya) and Cho-Shui (Taiwan) Rivers [*Burtin et al.*, 2008; *Hsu et al.*, 2011], or the hydrological conditions in the river channel at the location of the seismic stations were unknown, as in *Burtin et al.* [2011] where flow depth was only measured at the downstream end of the river, while several channels may have had flow during the time of record, all potentially with different and nondocumented local channel widths and depths.

Schmandt et al. [2013] reported seismic observations acquired during a controlled flood experiment with three main components in the seismic signal (see Figure 3 of *Schmandt et al.* [2013]). Two of these three components, with low-frequency peaks located between 0.5 and 10 Hz, were attributed to water flow-induced noise, as no hysteresis behavior could be observed with respect to river discharge at these frequencies. The third component, observed at higher frequencies (between 15 and 45 Hz), was identified as bedload, as the signal in this frequency range is characterized by a strong temporal intermittency and hysteresis relative to water level. At frequencies lower than 10 Hz, the authors suggested that the relatively high frequency peak centered around 6–7 Hz resulted from the breaking of waves occurring at the fluid-air interface, as large infrasound energy was also observed in the same frequency range. In contrast, the low-frequency peak occurring at several seconds of period (centered around 0.7 Hz) was proposed to result from fluid forces acting on the rough riverbed. In this context, we apply our physical model in order to determine whether some of these spectral features can be captured. Prior to performing model predictions, we introduce the river geometry and fluvial parameters, as well as ground seismic properties. All the parameters used below for model predictions are listed in Table 1.

4.1. River Parameters

The geometry of the river and its fluvial properties are inferred from the direct measurements provided by the U.S. Geological Survey [*Kieffer*, 1988, 1987]. Although the measurements reported therein were conducted more than 20 years before the seismic acquisitions of *Schmandt et al.* [2013], we assume that they still provide reasonable estimates of the current rapids configuration. This assumption is supported by the relative stability of the riverbed geometry there, as the riverbed is mainly made of big boulders anchored in the main stream and is not mobilized by the usual discharges reached in the Colorado River.

4.1.1. Channel Geometry

The riverbed slope angle θ is obtained from the water surface elevations provided in *Kieffer* [1988]. We estimate a river slope angle of about $\theta \approx 1.15°$ over the 100 m of the rapids section. Over the rapids section,

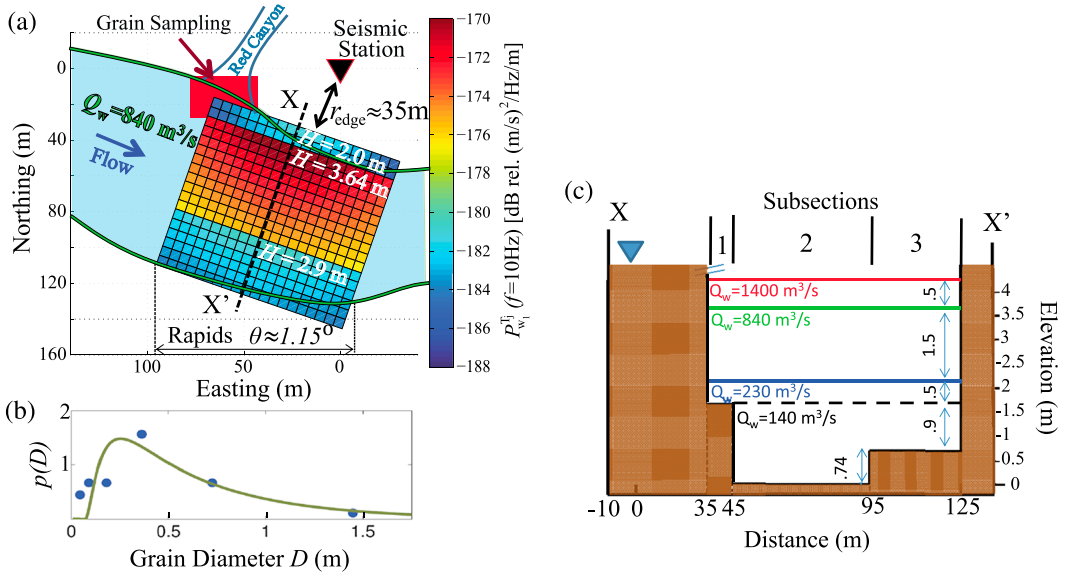

Figure 10. Channel geometry, riverbed grain sizes, and water flow depth associated with the Hance Rapids section of Grand Canyon. (a) Schematic of the river channel at Q_w = 840 m^3/s (green curve, modified from *Kieffer* [1988]) on top of which model results (5 m spaced color grid) show the contribution $P_{w_1}^{fj}$ (f = 10 Hz) (see equation (48)) of the different regions of the rapids in the resulting total turbulent flow-induced noise (green star in Figure 11). The small red rectangle indicates where the grain size distribution shown in inset was measured. The dashed black line between X and X' corresponds to where the cross section shown in Figure 10c is taken. (b) Measured (blue dots) and modeled (brown line) grain size distribution. The measurements are from *Kieffer* [1987], and the modeled distribution is calculated using D_{50} = 0.5 m and σ_g = 0.7 for the log-raised cosine distribution. (c) Riverbed topography and water flow depth values considered in model predictions (approximated from measurements of the $X - X'$ cross section shown in Figure 10a reported by *Kieffer* [1988]). The water flow depths when Q_w = 140 m^3/s (base flow depth) and Q_w = 840 m^3/s are constrained by direct observations [*Kieffer*, 1988], while H values at Q_w = 230 m^3/s and Q_w = 1400 m^3/s have been extrapolated by assuming a typical average velocity profile.

the channel width W varies from about 80 to 100 m for the various discharges (Figure 10a). As W does not play a key role in the model predictions, we take W to be constant with discharge. We set W = 90 m for Q_w > 140 m^3/s (Figure 10c).

The cross-stream topography is set from the cross-section transect $X - X'$ (see Figure 10a) provided in *Kieffer* [1988]. We assume that the cross-section $X - X'$ is representative of the reach. Based on *Kieffer* [1988], three subsections are defined with respect to a base water level where Q_w = 140 m^3/s (see Figure 10c). Subsection 1 is 10 m wide and has negligible flow velocities due to the fairly large and densely arranged boulders in that region. Thus, no flow is considered in that region for Q_w = 140 m^3/s, while only the excess water flow depth is accounted for at larger discharges. Subsection 2 is 50 m wide and has an average base flow depth of 1.64 m. Subsection 3 is 30 m wide and has an average base flow depth of about 0.9 m.

The boulder size distribution is reported in Figure 10b from measurements of *Kieffer* [1987], which were taken in the debris fan located downstream of Red Canyon (shown by the red rectangle in Figure 10a). We assume that these measurements are representative of the rapids section, and the "log"-raised cosine distribution $p(D)$ is adjusted using D_{50} = 0.5 m and σ_g = 0.7, resulting in k_s = 1.5 m.

4.1.2. Hydraulic Properties

The controlled flood experiment instrumented by *Schmandt et al.* [2013] had discharge variations from about 230 m^3/s to 1400 m^3/s. Direct observations of water level are reported in *Kieffer* [1988] for an intermediate discharge of Q_w = 840 m^3/s from which we estimate a 2 m flow depth increase from 140 m^3/s to 840 m^3/s of discharge (see Figure 10c). The extrema configurations of the control flood experiment instrumented by *Schmandt et al.* [2013] do not have direct water level observations. We therefore extrapolate the flow depth measurements performed at Q_w = 140 m^3/s and Q_w = 840 m^3/s to the configurations with Q_w = 230 m^3/s and Q_w = 1400 m^3/s by adding 0.5 m to both of the corresponding depth levels. A posteriori, using the water flow depth and the other channel information cited above, the total discharge

at each value of H can be approximated by using $U = 8.1\sqrt{g \sin\theta H}(H/k_s)^{1/6}$ [*Parker*, 1991] to describe the depth-average flow velocity.

4.2. Description of Rayleigh Waves

Since seismic wave parameters have not been measured on the river banks of Hance Rapids (HR), we describe surface wave velocities using the same parameters as previously for the Trisuli River, i.e., $v_{c0} = 2175$ m/s, $z_0 = 1000$, and $\xi = 0.48$ in equation (39). The value of Q_0 has been suggested by *Schmandt et al.* [2013] to plausibly be lower than 9, as $Q_0 = 9$ was found at <150 m depth in highly weathered granite [*Aster and Shearer*, 1991] and the seismic station was deployed on alluvium, i.e., on looser material. However, *Schmandt et al.* [2013] also suggested an alluvium layer of about 10 m deep at HR (see supporting information therein), under which bedrock is expected. We thus use $Q_0 = 9$, as surface waves are largely expected to propagate mostly in the bedrock layer at the relatively low frequencies of interest.

The distance from the edge of the river to the seismic station has been reported by *Schmandt et al.* [2013] to be about 38 m at low flow and 32 m at high flow. For simplicity, we do not account for changes in channel edge position with discharge and use the intermediate value of 35 m.

Since the station-to-river edge distance is similar to the river width, river flow sources located closer to the seismic station are expected to predominate compared to flow sources located further away. In addition, a "near-field" situation occurs at HR, since $rk < 1$ (where $k = 2\pi f/v_c$ is the seismic wave number and r is the distance between the source in the river and the receiver) for frequencies lower than about 3 Hz. To account for the relatively wide river breadth, we weight the flow sources with respect to their location by defining 5 m wide river transects in the along river direction. These transects span the entire rapids section, i.e., we define a number of transects $N_T = 18$, each of length $L_T = 100$ m. The total PSD $P^T_{w_1}$ of ground velocity can in that case be written as

$$P^T_{w_1}(f) = \sum_{j=1}^{N_T} \int_R P^{T_j}_{w_1}(f, \mathbf{x}_0)\mathrm{d}\mathbf{x}_0, \tag{48}$$

where $P^{T_j}_{w_1}(f, \mathbf{x}_0)$ denotes the contribution of ground motion generated per unit river length of transect (in units of $(\mathrm{m/s})^2/\mathrm{Hz/m}$) at location $\mathbf{x}_0$ and transect number j. To account for the near-field situation, we replace the term $\sqrt{\frac{2}{\pi kr}}$ commonly used to describe geometrical spreading for $rk >> 1$ (shown in the far-field Green's function of equation (37)) by the term $\left(1 + \left(\frac{\pi kr}{2}\right)^3\right)^{-1/6}$, which exhibits a finite value of 1 for $rk << 1$ while remaining similar to $\sqrt{\frac{2}{\pi kr}}$ in the far-field domain and thus approximates the expected Bessel function decay [*Aki and Richards*, 2002].

Under these modifications, by defining r_0^j as the smallest distance between the center of transect j and the seismic station, $P^T_{w_1}$ can be approximated by analogy with equation (42) as

$$P^T_{w_1}(f) \approx \sum_{j=1}^{N_T} \frac{40f^4(1+\xi)^2}{\rho_s(0)^2 v_c^6} \int_D S_F^j(f, D)\mathrm{d}D \int_{-L_T/2}^{L_T/2} \left(1 + \left(\frac{\pi k\sqrt{(r_0^j)^2 + y^2}}{2}\right)^3\right)^{-1/3} \exp\left(-\beta(r_0^j)\sqrt{1 + (y/r_0^j)^2}\right)\mathrm{d}y, \tag{49}$$

where β is defined in equation (46) and $S_F^j(f, D)$ corresponds to the PSD of force fluctuations defined per unit length along transect j (see equation (32)). One may note that the PSD $S_F^j(f, D)$ has been taken out of the along transect integral in equation (49), as it is constant over the transect section (e.g., due to constant flow depth, river slope, and other geometrical parameters along stream).

4.3. Forward Model Predictions

Turbulent flow-induced noise predictions are calculated over the entire rapids section by summing the contribution of all river transects using equation (48). As an example, the seismic power $P^{T_j}_{w_1}(f = 10\ \mathrm{Hz})$ calculated by unit length of transect and at discharge $Q_w = 840\ \mathrm{m^3/s}$ is shown for all transects in Figure 10a. The contribution of changes in flow depth along the cross-stream direction at HR primarily controls the predicted noise power, while the contribution of source-to-station distance plays a relatively minor role.

By summing up all pixel values shown in Figure 10a and multiplying the obtained value by the 5 m pixel length along the transect (similar to solving equation (49) for $f = 10$ Hz), we obtain the total noise shown

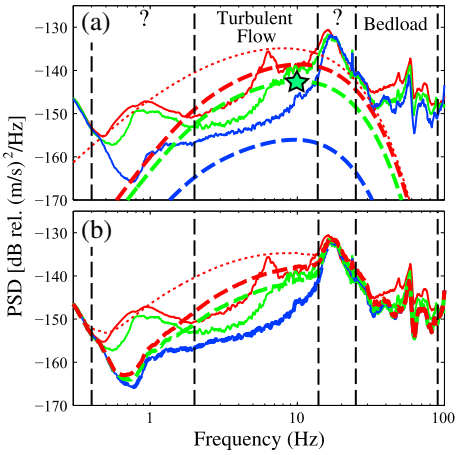

Figure 11. Model predictions of PSDs recorded at Hance Rapids of the Colorado River are compared with observations. (a) Observed (continuous lines) and modeled (thin and thick dashed lines) PSDs at the various discharges $Q_w = 230$ m^3/s (blue lines, $H = 2.14$ m), $Q_w = 840$ m^3/s (green lines, $H = 3.64$ m), and $Q_w = 1400$ m^3/s (red lines, $H = 4.14$ m). The thick dashed lines account for near-field and a finite length of the rapids (solving equation (49)), while the thin red dashed line does not, i.e., it uses a far-field Green's function and infinitely long rapids (solving equation (43) over infinitely long river transects). The green star indicates the configuration for which the contribution of the different regions within the rapids in generating the total water flow-induced noise power is shown in Figure 10a. (b) Similar to Figure 11a except that the PSD recorded at $Q_w = 230$ m^3/s has been added to all predicted PSDs following the interpretation supported by model predictions in Figure 11a that turbulent flow-induced noise is not significant at $Q_w = 230$ m^3/s. The vertical dashed black lines separate the different frequency ranges where the different source mechanisms are dominant.

as the green star in Figure 11a. The predicted PSDs obtained by repeating this calculation for all frequencies and all discharges are shown by the thick dashed lines in Figure 11a, on top of which observations are shown by the continuous lines (colors correspond). For comparison, the thin dashed red line indicates model prediction performed at $Q_w = 1400$ m^3/s by using the same flow depth values, but solving for turbulent flow-induced noise using equation (43) and the analytical (far-field and infinitely long river) approximation of equation (45) over each transect rather than the improved model of equation (49). It is important to note that, unlike *Schmandt et al.* [2013] who reported normalized PSDs (dB difference) relative to PSDs at the lowest discharge of $Q_w = 230$ m^3/s, we focus on the raw PSDs, i.e., on the PSDs that have not been normalized in any way. In the observed PSDs (continuous lines), the two peaks centered around 0.7 Hz and 6–7 Hz shown by *Schmandt et al.* [2013] at $Q_w = 1400$ m^3/s are not seen at the low discharge of $Q_w = 230$ m^3/s. Also, while seismic energy at large discharge is particularly enhanced at the two-peak frequencies described in *Schmandt et al.* [2013], the amplitude increase at larger discharges occurs over a relatively broad frequency range from 2 to 12 Hz.

At $Q_w = 230$ m^3/s, our model prediction does not capture the observed PSD (see Figure 11). However, as river discharge increases, the uppermost part of the frequency range affected by water flow is captured by our model predictions. Both the absolute amplitude and frequency dependence of our model predictions roughly agree with the observations at $Q_w = 840$ m^3/s and $Q_w = 1400$ m^3/s in the 2 to 12 Hz frequency range, i.e., within the frequency range with the high-frequency peak reported by *Schmandt et al.* [2013].

We remark that the infinitely long river assumption at HR (thin dashed line in Figure 11) is appropriate at high frequencies, i.e., at frequencies at which surface waves are strongly attenuated, but not at low frequencies, where a 10 dB overestimation is observed due to the misrepresentation of extra source contributions outside of the rapids section. One can also note the change of slope observed between the thin and the thick red dashed lines around 3 Hz, which is caused by the near-field situation accounted for by the thick red dashed line.

4.4. Interpretation

The agreement of our model predictions with the high-frequency peak reported by *Schmandt et al.* [2013] (2 to 12 Hz) suggests that this peak is caused by turbulent flow interacting with bed roughness rather than by breaking of river surface waves, as originally interpreted by *Schmandt et al.* [2013] on the basis of acoustic energy observed in the same frequency range. Since flow turbulence within the bed roughness is unlikely to generate acoustic noise in the air, we suggest that, by chance, another river flow acoustic source generates acoustic waves that propagate within a similar frequency range as that of the seismic noise caused by turbulent flow. The source mechanism for such a generated acoustic wave is not yet identified but could be related to breaking waves or imploding bubbles at the air-water interface.

Our model fails to reproduce the amplitude of the PSD recorded at $Q_w = 230$ m^3/s in Figure 11a. This disagreement is most likely because other sources of seismic noise energy are stronger than and overwhelm the turbulent flow-induced noise.

The peak centered at 17 Hz was interpreted by *Schmandt et al.* [2013] as a site effect due to resonance of the alluvium layer overlying bedrock. Regardless of whether the underlying source of noise is amplified or not by a site effect, this peak is unlikely to be caused by turbulent flow, since we would expect turbulent flow-induced noise to increase with discharge, irrespective of the specifics of the model. Since this is not observed, we believe that another source of noise (possibly bedload) is the cause of the peak at 17 Hz. Under such an expectation of a seismic noise source overwhelming turbulent flow-induced noise around 17 Hz, our model remains consistent with observations in that range, since it predicts a turbulent flow-induced noise power that is much smaller than observed around 17 Hz.

The low-frequency signal reported from 0.5 to 2 Hz by *Schmandt et al.* [2013] remains to be understood. *Schmandt et al.* [2013] interpreted this signal as resulting from fluid forces acting on the rough riverbed. We suggest that this low-frequency signal may result from standing waves. This hypothesis remains to be verified by future theoretical modeling and targeted measurements.

Following the interpretation provided above of a noise content recorded outside the 2 to 12 Hz frequency range that is attributed to other sources than turbulent flow, which one is overwhelmed by other sources within the 2 to 12 Hz frequency range at low flow, one can add the predicted turbulent flow-induced noise PSDs to the PSD recorded at low flow so that the frequency range resulting from the contribution of turbulent flow-induced noise can be better highlighted (see Figure 11b). There are however remaining discrepancies between modeled and observed PSDs. First, the modeled PSDs shown in Figure 11 exhibit a continuous decrease in power at decreasing frequency in the lower frequency part of the 2–12 Hz range, while the observed PSDs seem to flatten in that range. This misfit may be due to a misrepresentation of the frequency dependence of surface wave speeds or higher attenuation in our model (higher surface wave speeds or higher attenuation at lower frequencies would allow a better fit). Second, in the observations, the high-frequency peak centered around 6 to 8 Hz seems to shift toward lower frequencies as discharge increases. This effect could be reproduced by our model by accounting at increasing discharge for a migration of the maximum river depth location, which is a quantity on which model predictions heavily rely on (see Figure 10a). In particular, we may expect that the centrifugal force applied on the water column as the river undergoes a left turn at HR could result in larger flow depths toward the outside of the bend as discharge increases. Since the outside of the bend is located further away from the seismic station, this process could explain the migration toward lower frequencies at larger discharges.

5. Conclusions

We have developed a mechanistic model that accounts for the seismic noise caused by the interaction of turbulent flow with the riverbed. Force fluctuations applied in all directions on riverbed grains are explicitly accounted for from the description of the turbulent flow field, and the contribution of all riverbed grains in generating seismic surface waves is evaluated to reproduce the total ground velocity power recorded at a given, nearby, seismic station.

In agreement with previous observations [*Burtin et al.*, 2008, 2011; *Schmandt et al.*, 2013], the water flow-induced seismic noise is predicted to operate at lower frequencies than the seismic noise induced by a bedload signal. In the case of the Trisuli River in Nepal, we showed that a significant part of the seismic signal reported by *Burtin et al.* [2008] is attributable to turbulent flow. The hysteresis curve that attests for a sensitivity of seismic observations to bedload transport is in fact not only sensitive to bedload, and its shape is strongly influenced by the relative amplitude of turbulent flow-induced noise due to the additive properties of the noise sources (see Figures 2 and 3). Our model provides a noise base level from which the seismic noise level that is only attributed to bedload (and the associated bedload hysteresis curve) can be extracted from the total recorded signal to allow realistic bedload estimates in the future. For now, given the assumptions and approximations done in our model regarding river geometry, force properties, and ground structure, we estimated model prediction uncertainties of about an order of magnitude, i.e., $\approx$ 10 dB.

We demonstrated that the distance from the river to the seismic station, ground seismic properties, and hydrological characteristics such as the relative roughness of the flow and the river slope drastically change the relative amplitude and the frequency content of the seismic noise caused by turbulent flow versus seismic noise caused by bedload. Notably, the differences in the spectral signatures of turbulent flow-induced and bedload-induced forces at the riverbed are significant enough that these two processes can be

characterized independently by analyzing seismic records acquired at various distances from the river (see Figure 7). In particular cases, the turbulent flow and bedload sources are distinct on a single seismic record, for example, at the large flow discharges and short river-to-station distances at Hance Rapids of the Colorado River.

By using water flow depths and river geometries that reflect the Hance Rapids site where *Schmandt et al.* [2013] previously reported on a distinct water flow generated seismic noise source, we have shown that the absolute amplitudes and the frequency scaling of the seismic signal can be predicted. As riverbed stress is the main parameter that controls the absolute amplitude of the signal, this suggests that seismic observations can be used to invert for bed stress on the basis of this framework. Such a seismic monitoring technique is particularly promising for torrential steep rivers, where significant erosion rates, bedload transport, and channel migration cause direct and continuous measurements of water flow depth and riverbed stress to be particularly challenging. For now, given the order of magnitude uncertainty in current model predictions, we expect a factor of 1.5 uncertainty in flow depth estimates (or a factor of 1.2 in bed shear stress estimates) from seismic observations.

Besides the main and direct applications of the proposed theory to isolate the bedload-induced component of seismic noise by removing water flow-induced noise or to invert for flow depth or bed shear stress if these are unknown, the framework proposed in this study applied to specific seismic deployments may be used to better constrain the physics of the force fluctuations generated by the turbulent flow. In particular, this study relied on the various components of the fluctuating forces on a given grain all have similar amplitudes and spectral scaling. Moreover, we assumed that these force fluctuations are independent of each other. One could tackle the validity of these assumptions by using seismic noise correlations from dense seismic networks deployed along rivers. Such a study would allow one to relocate the turbulent flow sources and separate the contributions of the different turbulent forces applied in the different directions in generating seismic noise. When combined with accurate knowledge of ground seismic properties, such a deployment could allow the inversion of the entire spectral signature of the three components of force.

More generally, we find that interpreting the PSDs recorded at a given seismic station directly in terms of a source signature can be misleading, since the path effect associated with surface wave propagation strongly modifies the signal. Since seismic parameters play an important role in the model predictions, we encourage future seismological studies of rivers to investigate local ground properties from active (or passive) seismic experiments, without which quantitative interpretations of seismic signals will be limited. In cases where there is sufficiently complete knowledge of the ground seismic properties, the combination of the model proposed in this study with the bedload modeling framework proposed by *Tsai et al.* [2012] promises new and quantitative insights into the interplay between the local mechanical processes acting at the grain scale and channel morphology evolution.

Notation

A	Section area of the spherical riverbed grains (m^2) ($A = A_\perp = A_{//}$)
$A_\perp$	Grain section area normal to the flow direction (m^2) (defined in equation (1))
$A_\parallel$	Grain section area along the flow direction (m^2) (defined in equation (1))
$c_{\bar{u}}$	Coefficient relating the average flow velocity $\bar{u}_2$ with the bed shear velocity u_* (dimensionless) (see equation (8))
c_σ	Coefficient relating the turbulent flow velocity σ_{u_2} with the bed shear velocity u_* (dimensionless) (see equation (9))
C	Instantaneous fluid-grain friction coefficient under the isotropic conditions used (dimensionless) (see equation (27), $C = 0.5$ is used)
$C_1; C_L$	Instantaneous lift coefficient (dimensionless) (defined in equation (2))
$C_2; C_D$	Instantaneous drag coefficient (dimensionless) (defined in equation (2))
$C_3; C_C$	Instantaneous cross-stream coefficient (dimensionless)
$\bar{C}_D$	Average drag coefficient (dimensionless) (defined in equation (1))
$\bar{C}_L$	Average lift coefficient (dimensionless) (defined in equation (1))
dA	Subarea of A on which an incremental force is defined (m^2) (defined in equation (20))
df	Frequency band centered around frequency f (Hz)
dF_2	Incremental instantaneous drag force acting on area dA (N) (defined in equation (21))

dF_2'	Incremental fluctuating drag force acting on area dA (N) (defined in equation (22))
$d\bar{F}_2$	Incremental average drag force acting on area dA (N) (defined in equation (22))
D	Grain diameter (m) (see Figure 1)
D_{50}	Median grain size (m) (see Figure 1, see Table 1 for values used in model predictions)
E_{u_2}	PSD of streamwise velocities in wave number domain ($m^2\ s^{-2}\ (1/m)^{-1}$) (defined in equation (16))
f	Frequency of flow velocity, pressure and ground motion fluctuations (Hz)
f_w^{peak}	Peak frequency predicted from the water flow model (Hz) (see Figure 4)
f_b^{peak}	Peak frequency predicted from the bedload model (Hz) (see Figure 4)
f_{min}	Lower bound frequency of the inertial subrange (Hz) (see section 2.1)
f_{max}	Upper bound frequency of the inertial subrange (Hz) (see section 2.1)
f_c	Corner frequency of the transfer function χ_{fl} (Hz) (see equation (28))
F_i	Instantaneous fluid force applied along direction i (see equation (3))
$F_D; F_2$	Instantaneous drag force (N) (defined in equation (2))
$F_D'; F_2'$	Fluctuating drag force (N) (defined in equation (2))
$\bar{F}_D$	Average drag force (N) (defined in equation (1))
$\bar{F}_L$	Average lift force (N) (defined in equation (1))
g	Acceleration due to gravity ($m\ s^{-2}$) (set to 9.81 $m\ s^{-2}$)
G_{pi}	Green's function for a force applied along direction i and ground displacement along direction p (N^{-1} m) (defined in equation (3), formalized in section 2.3)
H	Depth of flow (m) (see Table 1)
H_0	Reference depth of flow (m) (see Figure 9)
I_1	Energy integral of the Rayleigh surface wave (kg) (defined in equation (35))
k	Wave number of the Rayleigh wave (m^{-1}) (see equation (34))
k_s	Roughness length of the riverbed (m) (set to $3D_{50}$)
k_w	Wave number of flow velocity fluctuations (m^{-1}) (defined in equation (16))
K	Kolmogorov constant (dimensionless) (defined in equation (16) set to 0.5)
l_c	Correlation length or mixing length (m) (set to k_s)
N_g	Number of grains per unit length of river per unit grain size (m^{-2}) (defined in equation (30))
N_T	Number of transects designed for Hance Rapids (dimensionless) (see equation (48), set to 18)
N_{ij}	Amplitude coefficient of the displacement Green's function for a force applied along direction j and a displacement evaluated along direction i (dimensionless) (see equation (36))
$p(D)$	Log-raised cosine distribution per unit grain size D (m^{-1}) (defined in *Tsai et al.* [2012])
$P_{w_p}^g$	PSD of ground velocity predicted along direction p for flow forces acting on a single grain g ($m^2\ s^{-2}\ Hz^{-1}$) (defined in equation (6))
$P_{w_p}^T$	Total PSD of ground velocity along direction p for river integrated flow forces ($m^2\ s^{-2}\ Hz^{-1}$) (defined in equation (7), formalized in equation (47))
$P_{w_p}^{T_j}$	PSD of ground velocity predicted at Hance Rapids along direction p for flow forces integrated over a unit length of transect T_j ($m^1\ s^{-2}\ Hz^{-1}$) (defined in equation (48)) (defined in equation (7), formalized in equation (43))
$P_{b_p}^T$	Total PSD of ground velocity predicted along direction p by the bedload model ($m^2\ s^{-2}\ Hz^{-1}$) (calculated from *Tsai et al.* [2012])
q_b	Bedload flux ($m^2\ s^{-1}$) (set from *Tsai et al.* [2012] for the Trisuli bedload predictions, otherwise scaled with q_{bc})
q_{bc}	Bedload flux at transport capacity ($m^2\ s^{-1}$) (defined in equation (47))
Q	Quality factor at a given frequency (dimensionless) (see equation (37))
Q_0	Quality factor at $f_0 = 1$ Hz (dimensionless) (either equal to 5 or 20 in section 3, or to values shown in Table 1 for predictions against data)
Q_w	Water discharge ($m^3\ s^{-1}$) (see section 4)
r	Station-to-source distance (m) (defined in equation (34))
r_0	Station-to-river distance (m) (defined in equation (46))
r_0^j	Station-to-transect j distance at Hance Rapids (m) (see section 4.2)
r_1	Rayleigh wave eigenfunction of vertical displacement (m) (see equation (34))
r_2	Rayleigh wave eigenfunction of horizontal displacement (m) (see equation (34))

R	Submerged specific density of sediment (dimensionless) (see equation (47), set to 1.8)
Re	Reynolds number (dimensionless) (see section 2.1)
S^g_{ab}	Cospectral density of velocities at two different locations a and b of A (N^2/Hz) (defined in equation (25))
S_{u_2}	PSD of streamwise velocities in the frequency domain ($m^2\ s^{-2}\ Hz^{-1}$) (defined in equation (17))
S_F	Isotropic PSD of flow forces per unit length of river and per unit grain size ($N^2\ m^{-2} Hz^{-1}$) (defined in section 2.4)
S^j_F	Isotropic PSD of flow forces per unit length of transect j and per unit grain size ($N^2\ m^{-2}\ Hz^{-1}$) (see section 4.2)
S_{F_i}	PSD of flow forces acting along direction i per unit length of river and per unit grain size ($N^2\ m^{-2}\ Hz^{-1}$) (defined in equation (7), formalized in equation (32))
$S^g_{F_i}$	PSD of flow forces acting along direction i and on a given grain g ($N^2\ Hz^{-1}$) (defined in equation (6), formalized in equation (27))
t	Time (s)
u_2	Instantaneous streamwise velocities ($m\ s^{-1}$) (defined in section 2.1)
u'_2	Fluctuating streamwise velocities ($m\ s^{-1}$) (defined in section 2.1)
$\bar{u}_2$	Average streamwise velocities ($m\ s^{-1}$) (defined in section 2.1, formulated in equation (8))
u_*	Bed shear velocity ($m\ s^{-1}$) (defined in equation (8), formalized in equation (41))
u^g_p	Ground velocity generated along direction p by fluid forces acting on grain g ($m\ s^{-1}$) (defined in equation (3))
U	Depth averaged velocity ($m\ s^{-1}$) (defined in section 4.1.2)
v_c	Phase speed of the Rayleigh wave ($m\ s^{-1}$) (defined in equation (39))
v_{c0}	Phase speed of the Rayleigh wave at frequency $f_0 = 1$ Hz ($m\ s^{-1}$) (see equation (39), set to 2175 $m\ s^{-1}$)
v_u	Group speed of the Rayleigh wave ($m\ s^{-1}$) (defined in equation (39))
v_s	Seismic shear wave speed ($m\ s^{-1}$) (varies with depth, see *Tsai and Atiganyanun* [2014])
W	River width (m) (see Table 1)
w_s	Settling velocity ($m\ s^{-1}$) (see section 3.2, calculated from *Ferguson and Church* [2004])
X_1	Elevation within the roughness layer (m) (see Figure 1)
X^{dA}_1	Coordinate of the center of subarea dA (m) (see equation (21))
X^r_1	Reference elevation at which the analysis is conducted (m) (set to $k_s/2$, see Figure 1)
$\mathbf{x}_0$	Reference coordinate vector of a given grain within the channel (m) (see equation (3))
$\mathbf{x}$	Reference coordinate vector of the seismic station (m) (see equation (3))
z	Depth in meter below ground surface (m) (see equation (2.3))
z_F	Depth below ground surface of the point source considered in the general Green's function definition (m) (see equation (34), set to 0)
z_S	Depth below ground surface of the seismic station location (m) (see equation (34), set to 0)
α	Exponent that expresses the grain size dependence of the critical value of Shields stress (dimensionless) (see equation (47), set to 0.9)
β	Function that accounts for inelastic attenuation in the infinitely long river approximation (dimensionless) (see equation (46))
γ_{ij}	Turbulent rate of strain evaluated along direction j for the velocity operating along direction i (s^{-1})
Γ_{12}	Macroscopic mean rate of strain in the water layer (Hz) (defined in equation (10), formalized in equation (13))
ϵ	Turbulent dissipation rate ($J\ kg^{-1} s^{-1}$) (defined in equation (11), formalized in equation (15))
η_{Kolmo}	Kolmogorov microscale (m) (see section 2.1)
η	Exponent characterizing quality factor increase with frequency (dimensionless) (see equation (40), set to 0)
ν	Kinematic viscosity ($m^2\ s^{-1}$) (see equation (11))

ϕ_D Function that accounts for the modulation of ground motion power by grain size (m^2) (see equation (44))

ψ_β Function that accounts for the modulation of ground motion power by the geometrical spreading and inelastic attenuation of the ground (dimensionless) (see equation (44))

θ River slope angle (degree) (see Table 1)

ρ_w Water density (kg m^{-3}) (set to 1500 kg m^{-3})

ρ_s Rock density (kg m^{-3}) (defined in section 2.3, varies with depth)

σ_g Standard deviation of the equivalent normal distribution of the log-raised cosine distribution (dimensionless) (see *Tsai et al.* [2012])

σ_{u_i} Turbulence intensity along direction i (m s^{-1}) (see equation (9))

$\sigma_{u_i,\max}$ Maximum turbulence intensity along direction i, measured at the roughness height (m s^{-1}) (we set $\sigma_{u_i}\left(X_1^r\right) = \sigma_{u_i,\max}$)

Σ_2^{ab} Cospectral density of force time series applied at two different locations a and b over a given grain (N^2/Hz) (defined in equation (23))

τ^* Shields stress (dimensionless) (see equation (47))

τ_{*c} Critical value of Shields stress (dimensionless) (see equation (47))

τ_{*c50} Critical value of Shields stress for grain size D_{50} (dimensionless) (see equation (47))

φ Source-station azimuth (radian) (see equation (34))

$\wp$ Turbulent production rate (J $kg^{-1}s^{-1}$) (defined in equation (10))

χ_{fl} Fluid admittance or transfer function between fluid velocity spectrum and pressure spectrum (dimensionless) (defined in equation (28))

ξ Exponent of the power law variation of Rayleigh wave velocities with frequency (see equation (39), set to 0.48)

ζ Function that accounts for the modulation of ground power by flow velocity changes operating within the bed roughness with changes of apparent roughness of the flow (dimensionless) (see equation (33))

Acknowledgments
We thank B. Schmandt for providing data and J.G. Venditti as well as J.-P. Avouac for interesting discussions. We thank two anonymous reviewers and D. Roth for helpful reviews. M.P.L acknowledges funding from the Terrestrial Hazards Observations and Reports Programs at Caltech and NSF grant EAR-1349115. F.G. was partially supported by funding from the Tectonics Observatory.

References

Achenbach, E. (1974), Vortex shedding from spheres, *J. Fluid Mech.*, *62*(02), 209–221, doi:10.1017/S0022112074000644.
Aki, K., and P. G. Richards (2002), *Quantitative Seismology,* 2nd ed., 700 pp., Univ. Sci., Sausalito, Calif.
Anderson, J. G., and S. E. Hough (1984), A model for the shape of the Fourier amplitude spectrum of acceleration at high frequencies, *Bull. Seismol. Soc. Am.*, *74*(5), 1969–1993.
Aster, R. C., and P. M. Shearer (1991), High-frequency borehole seismograms recorded in the San Jacinto Fault Zone, Southern California, Part 2. Attenuation and site effects, *Bull. Seismol. Soc. Am.*, *81*(4), 1081–1100.
Bagnold, R. A. (1966), An approach to the sediment transport problem from general physics, *U.S. Geol. Surv. Prof. Pap.*, *422-I*, I1–I37.
Bayazit, M. (1976), Free surface flow in a channel of large relative roughness, *J. Hydrol. Res.*, *14*(2), 115–126, doi:10.1080/00221687609499676.
Belleudy, P., A. Valette, and B. Graff (2010), Passive hydrophone monitoring of bedload in river beds: First trials of signal spectral analyses, *U. S. Geol. Surv. Sci. Invest. Rep.*, *2010*(5091), 67–84.
Bonnefoy-Claudet, S., C. Cornou, P.-Y. Bard, F. Cotton, P. Moczo, J. Kristek, and D. Fäh (2006), H/V ratio: A tool for site effects evaluation. Results from 1-D noise simulations, *Geophys. J. Int.*, *167*(2), 827–837, doi:10.1111/j.1365-246X.2006.03154.x.
Boore, D. M., and W. B. Joyner (1997), Site amplifications for generic rock sites, *Bull. Seismol. Soc. Am.*, *87*(2), 327–341.
Burtin, A., L. Bollinger, J. Vergne, R. Cattin, and J. L. Nábělek (2008), Spectral analysis of seismic noise induced by rivers: A new tool to monitor spatiotemporal changes in stream hydrodynamics, *J. Geophys. Res.*, *113*, B05301, doi:10.1029/2007JB005034.
Burtin, A., R. Cattin, L. Bollinger, J. Vergne, P. Steer, A. Robert, N. Findling, and C. Tiberi (2011), Towards the hydrologic and bed load monitoring from high-frequency seismic noise in a braided river: The torrent de St Pierre, French Alps, *J. Hydrol.*, *408*(12), 43–53, doi:10.1016/j.jhydrol.2011.07.014.
Carollo, F., V. Ferro, and D. Termini (2005), Analyzing turbulence intensity in gravel bed channels, *J. Hydraul. Eng.*, *131*(12), 1050–1061, doi:10.1061/(ASCE)0733-9429(2005)131:12(1050).
Curle, N. (1955), The influence of solid boundaries upon aerodynamic sound, *Proc. R. Soc. London A Math.*, *231*(1187), 505–514, doi:10.1098/rspa.1955.0191.
Defina, A., and A. C. Bixio (2005), Mean flow and turbulence in vegetated open channel flow, *Water Resour. Res.*, *41*, W07006, doi:10.1029/2004WR003475.
Díaz, J., M. Ruíz, L. Crescentini, A. Amoruso, and J. Gallart (2014), Seismic monitoring of an Alpine mountain river, *J. Geophys. Res. Solid Earth*, *119*, 3276–3289, doi:10.1002/2014JB010955.
Egholm, D. L., M. F. Knudsen, and M. Sandiford (2013), Lifespan of mountain ranges scaled by feedbacks between landsliding and erosion by rivers, *Nature*, *498*(7455), 475–478, doi:10.1038/nature12218.
Einstein, H., and N. L. Barbarossa (1952), River channel roughness, *Trans. Am. Soc. Civ. Eng.*, *117*, 1121–1146.
Erickson, D., and D. McNamara (2004), Frequency-dependent Lg Q within the continental united states, *Bull. Seismol. Soc. Am.*, *94*, 1630–1643, doi:10.1785/012003218.
Ferguson, R. I., and M. Church (2004), A simple universal equation for grain settling velocity, *J. Sediment. Res.*, *74*(6), 933–937, doi:10.1306/051204740933.
Fernandez Luque, R., and R. Van Beek (1976), Erosion and transport of bed-load sediment, *J. Hydraul. Res.*, *14*(2), 127–144, doi:10.1080/00221687609499677.

Govi, M., F. Maraga, and F. Moia (1993), Seismic detectors for continuous bed load monitoring in a gravel stream, *Hydrol. Sci. J.*, *38*(2), 123–132, doi:10.1080/02626669309492650.
Howard, A. D., and G. Kerby (1983), Channel changes in badlands, *Geol. Soc. Am. Bull.*, *94*(6), 739–752, doi:10.1130/0016-7606(1983)94<739:CCIB>2.0.CO;2.
Hsu, L., N. J. Finnegan, and E. E. Brodsky (2011), A seismic signature of river bedload transport during storm events, *Geophys. Res. Lett.*, *38*, L13407, doi:10.1029/2011GL047759.
Kamphuis, J. W. (1974), Determination of sand roughness for fixed beds, *J. Hydraul. Res.*, *12*(2), 193–203, doi:10.1080/00221687409499737.
Kieffer, S. W. (1987), The rapids and waves of the Colorado River, Grand Canyon, Arizona, *Tech. Rep. D-5*, Denver, Colo.
Kieffer, S. W. (1988), Hydraulic map of Hance Rapids, Grand Canyon, Arizona, *Tech. Rep. I - 1897-C*, U. S. Geol. Surv., Denver, Colo.
Kline, S. J., W. C. Reynolds, F. A. Schraub, and P. W. Runstadler (1967), The structure of turbulent boundary layers, *J. Fluid Mech.*, *30*(04), 741–773, doi:10.1017/S0022112067001740.
Kolmogorov, A. (1941), The local structure of turbulence in incompressible viscous fluid for very large Reynolds' numbers, *Akad. Nauk SSSR Dokl.*, *30*, 301–305.
Lamb, M. P., W. E. Dietrich, and L. S. Sklar (2008a), A model for fluvial bedrock incision by impacting suspended and bed load sediment, *J. Geophys. Res.*, *113*, F03025, doi:10.1029/2007JF000915.
Lamb, M. P., W. E. Dietrich, and J. G. Venditti (2008b), Is the critical shields stress for incipient sediment motion dependent on channel-bed slope?, *J. Geophys. Res.*, *113*, F02008, doi:10.1029/2007JF000831.
Legleiter, C. J., T. L. Phelps, and E. E. Wohl (2007), Geostatistical analysis of the effects of stage and roughness on reach-scale spatial patterns of velocity and turbulence intensity, *Geomorphology*, *83*(34), 322–345, doi:10.1016/j.geomorph.2006.02.022.
Lighthill, M. J. (1952), On sound generated aerodynamically. I. General theory, *Proc. R. Soc. London A Math.*, *211*(1107), 564–587, doi:10.1098/rspa.1952.0060.
Manning, R. (1891), On the flow of water in open channels and pipes, *Trans. Inst. Civ. Eng. Irel.*, *20*, 161–207.
Marquis, G., and A. G. Roy (2013), From macroturbulent flow structures to large-scale flow pulsations in gravel-bed rivers, in *Coherent Flow Structures at Earth's Surface*, edited by J. G. Venditti et al., pp. 243–259, Wiley-Blackwell, Chichester, West Sussex, U. K.
McLean, S. R., and V. I. Nikora (2006), Characteristics of turbulent unidirectional flow over rough beds: Double-averaging perspective with particular focus on sand dunes and gravel beds, *Water Resour. Res.*, *42*, W10409, doi:10.1029/2005WR004708.
Nakagawa, H., and I. Nezu (1981), Structure of space-time correlations of bursting phenomena in an open-channel flow, *J. Fluid Mech.*, *104*, 1–43, doi:10.1017/S0022112081002796.
Naudascher, E., and D. Rockwell (2005), *Flow-Induced Vibrations: An Engineering Guide*, Dover Publications, Mineola, New York.
Nelson, J. M., N. W. Schmeeckle, and S. L. Shreve (2001), Turbulence and particle entrainment, in *Bravel-Bed River V*, edited by M. P. Morsley, pp. 221–240, N. Z. Hydrol. Soc., Wellington, New Zealand.
Nezu, I., and H. Nakagawa (1993), *Turbulence in Open-Channel Flows*, Balkema, Rotterdam; Brookfield.
Nezu, I., and W. Rodi (1986), Openchannel flow measurements with a laser Doppler anemometer, *J. Hydraul. Eng.*, *112*(5), 335–355, doi:10.1061/(ASCE)0733-9429(1986)112:5(335).
Nikora, V. (2011), Hydrodynamics of gravel-bed rivers: Scale issues, in *Gravel Bed Rivers 6: From Process Understanding to River Restoration: 11*, 1st ed., edited by H. Habersack, H. Piegay, and M. Rinaldi, pp. 61–81, Elsevier Science, Amsterdam, Netherlands.
Nikora, V., and D. Goring (2000), Flow turbulence over fixed and weakly mobile gravel beds, *J. Hydraul. Eng.*, *126*(9), 679–690, doi:10.1061/(ASCE)0733-9429(2000)126:9(679).
Nikora, V., D. Goring, I. McEwan, and G. Griffiths (2001), Spatially averaged open-channel flow over rough bed, *J. Hydraul. Eng.*, *127*(2), 123–133, doi:10.1061/(ASCE)0733-9429(2001)127:2(123).
Nikora, V., K. Koll, I. McEwan, S. McLean, and A. Dittrich (2004), Velocity distribution in the roughness layer of rough-bed flows, *J. Hydraul. Eng.*, *130*(10), 1036–1042, doi:10.1061/(ASCE)0733-9429(2004)130:10(1036).
Norberg, C. (2003), Fluctuating lift on a circular cylinder: Review and new measurements, *J. Fluid Struct.*, *17*(1), 57–96, doi:10.1016/S0889-9746(02)00099-3.
Parker, G. (1990), Surface-based bedload transport relation for gravel rivers, *J. Hydraul. Res.*, *28*(4), 417–436, doi:10.1080/00221689009499058.
Parker, G. (1991), Selective sorting and abrasion of river gravel. II: Applications, *J. Hydraul. Eng.*, *117*(2), 150–171, doi:10.1061/(ASCE)0733-9429(1991)117:2(150).
Raupach, M. R., R. A. Antonia, and S. Rajagopalan (1991), Rough-wall turbulent boundary layers, *Appl. Mech. Rev.*, *44*(1), 1–25, doi:10.1115/1.3119492.
Rickenmann, D., and A. Recking (2011), Evaluation of flow resistance in gravel-bed rivers through a large field data set, *Water Resour. Res.*, *47*, W07538, doi:10.1029/2010WR009793.
Rickenmann, D., J. M. Turowski, B. Fritschi, A. Klaiber, and A. Ludwig (2012), Bedload transport measurements at the erlenbach stream with geophones and automated basket samplers, *Earth Surf. Processes Landforms*, *37*(9), 1000–1011, doi:10.1002/esp.3225.
Roy, A. G., T. Buffin-Blanger, H. Lamarre, and A. D. Kirkbride (2004), Size, shape and dynamics of large-scale turbulent flow structures in a gravel-bed river, *J. Fluid Mech.*, *500*, 1–27, doi:10.1017/S0022112003006396.
Roth, D. L., N. J. Finnegan, E. E. Brodsky, K. L. Cook, C. P. Stark, and H. W. Wang (2014), Migration of a coarse fluvial sediment pulse detected by hysteresis in bedload generated seismic waves, *Earth Planet. Sci. Lett.*, *404*, 144–153, doi:10.1016/j.epsl.2014.07.019.
Sarpkaya, T. (1979), Vortex-induced oscillations: A selective review, *J. Appl. Mech.*, *46*(2), 241–258, doi:10.1115/1.3424537.
Scheingross, J. S., E. W. Winchell, M. P. Lamb, and W. E. Dietrich (2013), Influence of bed patchiness, slope, grain hiding, and form drag on gravel mobilization in very steep streams, *J. Geophys. Res. Earth Surf.*, *118*, 982–1001, doi:10.1002/jgrf.20067.
Schlichting, H. (1979), *Boundary-Layer Theory*, McGraw-Hill, New York.
Schmandt, B., R. C. Aster, D. Scherler, V. C. Tsai, and K. Karlstrom (2013), Multiple fluvial processes detected by riverside seismic and infrasound monitoring of a controlled flood in the Grand Canyon, *Geophys. Res. Lett.*, *40*, 4858–4863, doi:10.1002/grl.50953.
Schmeeckle, M. W. (2014), Numerical simulation of turbulence and sediment transport of medium sand, *J. Geophys. Res. Earth Surf.*, *119*, 1240–1262, doi:10.1002/2013JF002911.
Schmeeckle, M. W., and J. M. Nelson (2003), Direct numerical simulation of bedload transport using a local, dynamic boundary condition, *Sedimentology*, *50*(2), 279–301, doi:10.1046/j.1365-3091.2003.00555.x.
Schmeeckle, M. W., J. M. Nelson, and R. L. Shreve (2007), Forces on stationary particles in near-bed turbulent flows, *J. Geophys. Res.*, *112*, F02003, doi:10.1029/2006JF000536.
Sklar, L. S., and W. E. Dietrich (2004), A mechanistic model for river incision into bedrock by saltating bed load, *Water Resour. Res.*, *40*, W06301, doi:10.1029/2003WR002496.
Taylor, G. I. (1938), The spectrum of turbulence, *Proc. R. Soc. London*, *164*(919), 476–490, doi:10.1098/rspa.1938.0032.

Tennekes, H., and J. L. Lumley (1972), *A First Course in Turbulence*, The MIT, Cambridge, London, U. K.
Tsai, V. C., and S. Atiganyanun (2014), Green's functions for surface waves in a generic velocity structure, *Bull. Seismol. Soc. Am.*, *104*(5), doi:10.1785/0120140121.
Tsai, V. C., B. Minchew, M. P. Lamb, and J.-P. Ampuero (2012), A physical model for seismic noise generation from sediment transport in rivers, *Geophys. Res. Lett.*, *39*, L02404, doi:10.1029/2011GL050255.
Tsujimoto, T. (1991), Bed-load transport in steep channels, in *Fluvial Hydraulics of Mountain Regions*, edited by P. A. Armanini, and P. G. D. Silvio, pp. 89–102, no. 37 in Lecture Notes in Earth Sciences, Springer, Berlin, Heidelberg.
Turowski, J., and D. Rickenmann (2011), Measuring the statistics of bed-load transport using indirect sensors, *J. Hydraul. Eng.*, *137*(1), 116–121, doi:10.1061/(ASCE)HY.1943-7900.0000277.
Venditti, J. G., J. L. Best, M. Church, and R. J. Hardy (2013), *Coherent Flow Structures at Earth's Surface,* 1st ed., Wiley-Blackwell, Chichester, West Sussex, U. K.
Vickery, B. J. (1966), Fluctuating lift and drag on a long cylinder of square cross-section in a smooth and in a turbulent stream, *J. Fluid Mech.*, *25*(03), 481–494, doi:10.1017/S002211206600020X.
Wang, J., Z. Dong, C. Chen, and Z. Xia (1993), The effects of bed roughness on the distribution of turbulent intensities in open-channel flow, *J. Hydraul. Res.*, *31*(1), 89–98, doi:10.1080/00221689309498862.
Whipple, K. X. (2004), Bedrock rivers and the geomorphology of active orogens, *Annu. Rev. Earth Planet. Sci.*, *32*(1), 151–185, doi:10.1146/annurev.earth.32.101802.120356.
Whipple, K. X., G. S. Hancock, and R. S. Anderson (2000), River incision into bedrock: Mechanics and relative efficacy of plucking, abrasion, and cavitation, *Geol. Soc. Am. Bull.*, *112*(3), 490–503, doi:10.1130/0016-7606(2000)112<490:RIIBMA>2.0.CO;2.
Wiberg, P. L., and J. D. Smith (1991), Velocity distribution and bed roughness in high-gradient streams, *Water Resour. Res.*, *27*(5), 825–838, doi:10.1029/90WR02770.
Yalin, M. S. (1992), *River Mechanics* 1st ed., Pergamon Press, Oxford, New York.
Yuan, Z., and E. E. Michaelides (1992), Turbulence modulation in particulate flows: A theoretical approach, *Int. J. Multiphase Flow*, *18*(5), 779–785, doi:10.1016/0301-9322(92)90045-I.